SCIENTIFIC Publishing Limited

Journal of Hydrological Ecology and Water Security
https://ojs.ukscip.com/index.php/jhews

Article

Application of HEC-RAS for the Study of Sediment Continuity in the Clain River (Poitiers, France)

Alaa Ghzayel and Anthony Beaudoin *

FTC Department, Pprime Institute, University of Poitiers, 86073 Poitiers, France
* Correspondence: anthony.beaudoin@univ-poitiers.fr

Received: 20 April 2025; **Revised:** 20 April 2025; **Accepted:** 26 April 2025; **Published:** 5 May 2025

Abstract: Research on sediment transport has focused on large dams, whose impacts are more visibly dramatic. The impacts of low-head dams, which are smaller and more numerous, have received less attention. It is partly due to the challenges of modeling sediment transport in these environments, which requires high-resolution data on flow dynamics and sediment properties. This work shows that there are tools allowing the acquisition of these hydrometric data and that the hydro-morphodynamic models can integrate it. The study site is the Clain river flowing through the Grand Poitiers municipality in the Vienne department (France), where low-head dams are installed at two key sites, Îlot Tison and Saint-Benoît, which pose potential barriers to sediment continuity. The hydro-morphodynamics of the Clain river are studied by means of the software HEC-RAS. The numerical simulations, performed in this work, show that the software HEC-RAS uses water flow and sediment transport equations tailored to specific conditions of the Clain river, a plain river with low-head dams. The robustness of the turbulent model and sediment transport laws present in the software HEC-RAS was checked for this river type. These numerical simulations allowed us to elucidate the hydro-morphodynamic impacts of two low-head dams present at the Saint-Benoît and Îlot Tison sites, on the Grand Poitiers municipality. For specific discharges exceeding the mean specific discharge of the Clain river, the low-head dams are bypassed. For specific discharges below the mean specific discharge of the Clain river, disturbances in water flow and sediment transport occur locally around these low-head dams. The occurrence of two phenomena, erosional narrowing and widening, depends on the height of the removal dam, the specific discharge, and the volume of stored sediments upstream of the removal dam. Removing these two low-head dams doesn't disturb the hydro-morphodynamics of the Clain river at the large scale.

Keywords: Sediment Transport; Low-Head Dams; Hydro-Morphodynamic Modeling; Hydrometric Data; HEC-RAS Software

1. Introduction

The continuity of sediment transport in river systems is fundamental to maintaining natural hydro-morphodynamic processes, which are vital for biodiversity, water quality, and overall river health [1,2]. Sediment transport governs the erosion, deposition, and formation of riverbeds, banks, and associated habitats, playing a key role in ecosystem functioning and riverine landscape evolution [3,4]. Disruption of these processes can result in significant ecological and geomorphological consequences, such as habitat degradation, altered sediment composition, and destabilized river morphology [5,6].

Anthropogenic structures, such as weirs and dams, are among the most common causes of sediment transport disruption in regulated rivers. These structures act as physical barriers, impeding the natural flow of sediments

both upstream and downstream [7,8]. The cumulative impacts of these barriers have prompted extensive research into the hydro-morphodynamic alterations they induce and the development of mitigation strategies to restore sediment continuity and ecological balance [9,10].

France's river systems exemplify these challenges, with approximately 60,000 hydraulic structures segmenting river networks, a substantial proportion of which are low-head dams [11]. These structures that act like barriers that do not exceed the elevation of the riverbanks and allow flow over their crests, accounting for 81% of France's total number of dams [12,13], are often referred to as weirs, check dams, or small dams in scientific literature [13,14]. Low-head dams influence river dynamics by creating upstream zones of reduced flow velocity, leading to sediment deposition, and downstream zones of accelerated flow, often resulting in scouring and sediment depletion [15,16]. This disruption of natural sediment transport can cause sediment accumulation upstream and loss of sediment diversity downstream, with significant ecological consequences [17, 18]. Moreover, these effects compound over time, altering riverine habitats and reducing their capacity to support aquatic biodiversity [19,20].

Research on sediment transport has traditionally focused on large dams, whose impacts are more visibly dramatic and have been studied extensively over the past decades [7, 8, 21–23]. Large dams often cause significant sediment trapping in reservoirs, leading to downstream sediment deficits and altered channel morphology [21,24]. However, the impacts of low-head dams, which are smaller and more numerous, have received comparatively less attention despite their cumulative effects on river systems [14,16,25].

Low gradient river systems, which are sensitive to even minor disruptions, remain understudied despite their ecological significance [26]. Several studies have highlighted the localized impacts of low-head dams on sediment transport. For example, Kondolf et al. documented how such structures cause upstream sediment accumulation, which can smother spawning habitats and reduce benthic organism diversity [15]. Similarly, research by Schmutz and Moog emphasized how low-head dams disrupt sediment continuity, leading to scouring downstream and reduced sediment heterogeneity [10]. These studies underscore the importance of addressing the hidden effects of small barriers, which collectively have a profound influence on river health.

Despite these findings, significant gaps remain in understanding the broader hydro-morphodynamic implications of low-head dams. This knowledge gap is partly due to the challenges of modeling sediment transport in these environments, which require high-resolution data on flow dynamics and sediment properties [16,27,28]. To address this gap, hydro-morphodynamic modeling has emerged as a powerful tool for analyzing sediment transport in modified river systems. Software like HEC-RAS (Hydrologic Engineering Center's River Analysis System) enable researchers to simulate complex sediment transport dynamics by integrating field data on flow velocity and sediment granulometry with sediment transport equations tailored to specific river conditions [16, 29]. Recent studies highlight the potential of HEC-RAS in predicting sediment deposition, erosion, and transport patterns in the presence of hydraulic structures [30,31].

The software HEC-RAS is part of the large family of hydro-morphodynamic models based on Shallow-Water equations [32]. In the natural environments such as lakes, rivers, estuaries, and coastal shores, these equations describe the water flow with a free surface more or less accurately compared to the 3D Navier-Stokes equations, depending on whether turbulence is taken into account or not [33]. The hydro-morphodynamic models built with the classic Shallow-Water equations are not suitable for water flows with high fluctuating motions inducing turbulence [34]. To introduce turbulence into the Shallow-Water equations, the starting point is to apply Reynolds decomposition to the velocity components in the 3D Navier-Stokes equations [35]. In the averaged 3D Navier-Stokes equations, the averages of velocity components and the Reynolds stress tensor appear [36,37]. To close the system, it requires introducing equations for the Reynolds stress tensor [38]. The difference between the hydro-morphodynamics models, such as the software HEC-RAS, is the level of complexity involved in writing these equations. The first-order models use the Boussinesq assumption that relates the Reynolds stress tensor to the average strain by introducing the turbulent viscosity. The turbulent viscosity can then be estimated using the classical Prandtl hypothesis [38] or the k-ε and k-ω models [39,40]. The second-order models solve the Reynolds stress tensor transport equation by introducing models for terms that cannot be calculated directly [40,41]. With two options for modeling turbulence, the question arises as to under what flow conditions, characterized by an adimensional number, the Froude number, each approach should be used [34,41]. The works by Ngatcha et al. show that the second option should be used for flows with $Fr > 1$, as in the cases of hydraulic jumps and dam breaks [34,41]. Entering into the first-order models, the software HEC-RAS introduces the turbulence in the Shallow-Water equations using

the Smagorinsky model to estimate the turbulent viscosity [42]. For the sediment transport, the majority of hydro-morphodynamic models combine the Shallow-Water and Exner equations [16]. The software HEC-RAS does the same thing [43]. The recent works by Ngatcha et al. show that this coupling of Shallow-Water and Exner equations may be faulty to describe the sediment transport in flows with high fluctuating motions [34,44,45]. Over high slopes of the topography, high fluctuations of flow generate turbulence. It is a distorsion phenomenon. There is also the phase-lag phenomenon. The difference between hydrodynamic time and sedimentary time can be explained by the difference in water and bottom velocities. Having no turbulence terms, the classic Exner equation cannot describe the two phenomena, distorsion and phase-lag. In 2025, Ngatcha et al. proposed to modify the Exner equation by including the phase-lag effect and arbitrary slope sediment beds. This new hydro-morphodynamic model has been tested in the dambreak case, where the failure of a dam generates a flow with high turbulence, inducing high erosion of the bed behind the dam [45]. In light of recent advancements in Shallow-Water theory and sediment transport theory, it is important to verify the robustness of modeling based on classic hydro-morphodynamic models, such as the software HEC-RAS, to describe the water flow and the sediment transport in the rivers.

This study focuses on the Clain river flowing through the Grand Poitiers municipality in the Vienne department (France), where low-head dams installed at two key sites, Îlot Tison and Saint-Benoît, pose potential barriers to sediment continuity. It is not known whether these structures alter flow velocities, sediment deposition, and erosion patterns, thereby disrupting the natural sediment transport processes along the river's length. Although previous research has examined the impacts of weirs on water flow [16,46], their specific influence on sediment transport continuity in low-gradient rivers like the Clain river remains poorly understood. By integrating hydrometric data, such as ADCP flow velocity data and sediment granulometry, with HEC-RAS modeling, this research aims to elucidate the hydro-morphodynamic impacts of these low-head dams under varying flow scenarios.

Restoration efforts have increasingly focused on mitigating the effects of hydraulic barriers through strategies such as dam removal, sediment management, and riverbank stabilization [9, 47]. For instance, studies on dam removal have demonstrated the potential for rapid sediment redistribution and habitat recovery, as documented by Doyle et al. in their work on the Elwha river [27]. However, the outcomes of such interventions vary depending on site-specific conditions, including river gradient, sediment load, and flow regime [25].

In this study, two primary scenarios are simulated at each site, Îlot Tison and Saint-Benoît, using the software HEC-RAS: the current state with intact weirs and a hypothetical state without weirs, for various specific discharges, Q = 8 m^3/s (low flow), 25 m^3/s (median flow), and 156 m^3/s (10-year return period flood flow). By comparing these scenarios, the study assesses whether the low-head dams disrupt sediment transport continuity or lead to localized sediment accumulation. In this work, there are three objectives: (1) to integrate hydrometric data, such as ADCP flow velocity data and sediment granulometry, with HEC-RAS modeling, (2) to evaluate the robustness of the turbulent model and sediment transport laws present in the software HEC-RAS to describe the water flow and the sediment transport in the Clain river, (3) to assess the hydro-morphodynamic impacts of low-head dams of the Clain river under different flow conditions.

Additionally, large-scale scenarios encompassing the area from Saint-Benoît to Îlot Tison at a specific discharge of 25 m^3/s are analyzed. Initial fieldwork involves determining the grain size distribution of the riverbed sediments through a series of sediment sampling along the river and conducting sieve analysis and laser granulometry measurements. This grain size distribution is a critical parameter for calibrating the software HEC-RAS. Flow velocity measurements obtained using ADCP and current meters, along with specific discharge and water depth data from the Pont-Neuf hydraulic station on the Clain river, are used to validate and refine the hydro-morphodynamic modeling.

The structure of the paper is as follows. In Section II, we present the hydrometric data acquired in the field and used in the calibration of the hydro-morphodynamic modeling. They are composed of the sediment bed granulometry, the flow velocity, and the DTM (Digital Terrain Model) maps. For each hydrometric data, the material, the procedure, and the analysis are described. In Section III, we present the software HEC-RAS used for the hydro-morphodynamic modeling. The physical and numerical models used in the software HEC-RAS are described. In section IV, the calibration, validation, and scenario development of the hydro-morphodynamic modeling are described. In Section V, we present the analysis of numerical results obtained with the software HEC-RAS. Two observation scales are used: the local scale on the low-head dams located at the Îlot Tison and Saint-Benoît sites, and the large scale between these two sites. The last section is devoted to the conclusions and perspectives on the work.

2. Hydrometric Data

2.1. Sediment Bed Granulometry

To initialize the sediment model within the software HEC-RAS, knowledge of the sediment granulometry of the river bed is crucial. This granulometry gives the mass proportion of each sediment size class *d*. In the software HEC-RAS, this granulometry serves as a surface layer on the bathymetry, enabling the estimation of solid discharge for each sediment size class *d* [48].

The Clain river has a sinuous bed in its upstream part with numerous meanders and an average slope of 3‰. Its downstream part is characterized by a low slope, less than 0.8‰ [49,50]. By considering the classification of channel patterns given by Brice and Blodgett, the Clain river is an equiwidth channel presenting degrees of braiding and anabranching lower [51]. By considering the classification of alluvial channels given by Schumm, the Clain river is a channel type with a mixed load. In relation to these two classifications, the bed of the Clain river is composed of sand near banks and gravel near riffles [52].

In this work, the granulometric measurements are limited to surface measurements [53–55]. Using a boat, sediment samples were taken along the Clain, with a higher density of samples at the Îlot Tison and Saint-Benoît sites (see **Figure 1a**). To sample river sediments, the following equipment is used: a sediment corer, a shovel, and a Van Veen grab sampler. Using a 30 kg corer in deep areas proved to be difficult and inefficient, so it was abandoned after trials. For shallow parts of the river with direct access, a shovel was used to sample sediments directly from the bed. For deeper parts of the river, the 2L Van Veen grab sampler (surface area of 250 cm^2, approximately 10 kg) was used (see **Figure 1b** [56]). It consists of two semi-circular stainless steel jaws. The sampler is lowered slowly until it touches the riverbed. Once it has touched the bottom, the rope is pulled to close the jaws and trap the sediments inside. This equipment allows only to collect the sand [54,55].

(**a**) (**b**) (**c**) (**d**)

Figure 1. Equipment used to measure the sediment granulometry. (**a**) boat; (**b**) Van Veen sampler; (**c**) oven; (**d**) sieve column.

The next phase involves drying these samples in an oven at a temperature of 105 °C for 24 h (see **Figure 1c**). After drying, the bulk density of the sample is determined according to the method of water displacement. A sieving

analysis is then performed on the dry sample to deduce the mass proportion retained on each sieve, resulting in a granulometric curve that presents the cumulative passing percentage *P* for each sediment size class *d* (see **Figure 1d**) [53–55]. As shown in **Figure 2b**, the upstream samples, from 1 to 6 at the Saint-Benoît site, are composed of 60 to 70% coarse sand. Meanwhile, downstream at the Îlot Tison site, the coarse sand is around 20% for the samples 14, 15, and 16. **Figure 2a** presents two examples of sediment samples. In **Figure 3**, the granulometric curves, samples 1 to 6, are from upstream and are composed of coarse sand and a small fraction of gravel, which can vary between 1% and 10%. Meanwhile, downstream, the granulometric curves, samples 14, 15, and 16, show that the samples are mainly composed of fine sand (45%), medium sand (35%), and coarse sand (20%).

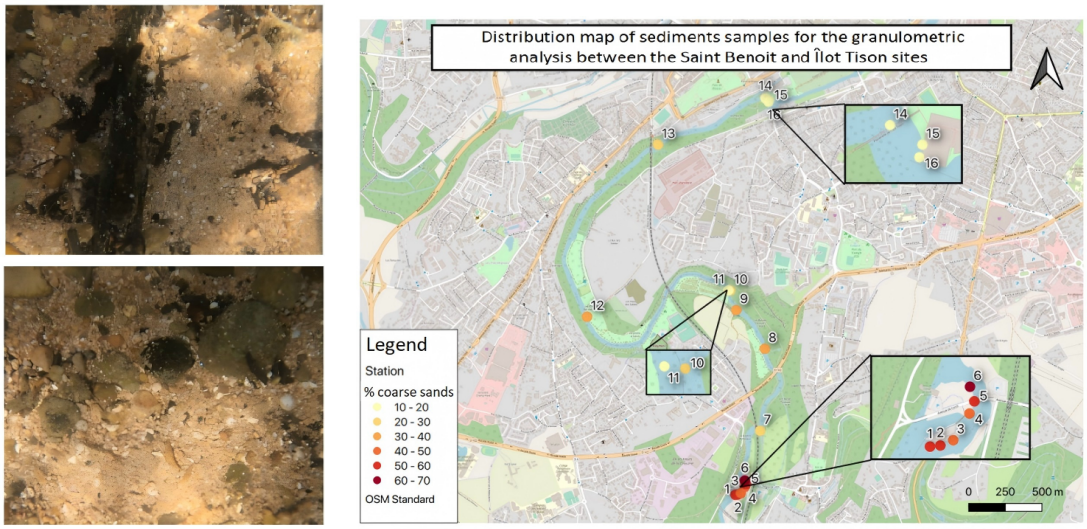

(**a**) (**b**)

Figure 2. (**a**) Example of sediment samples; (**b**) Distribution map of sediment samples along the Clain river.

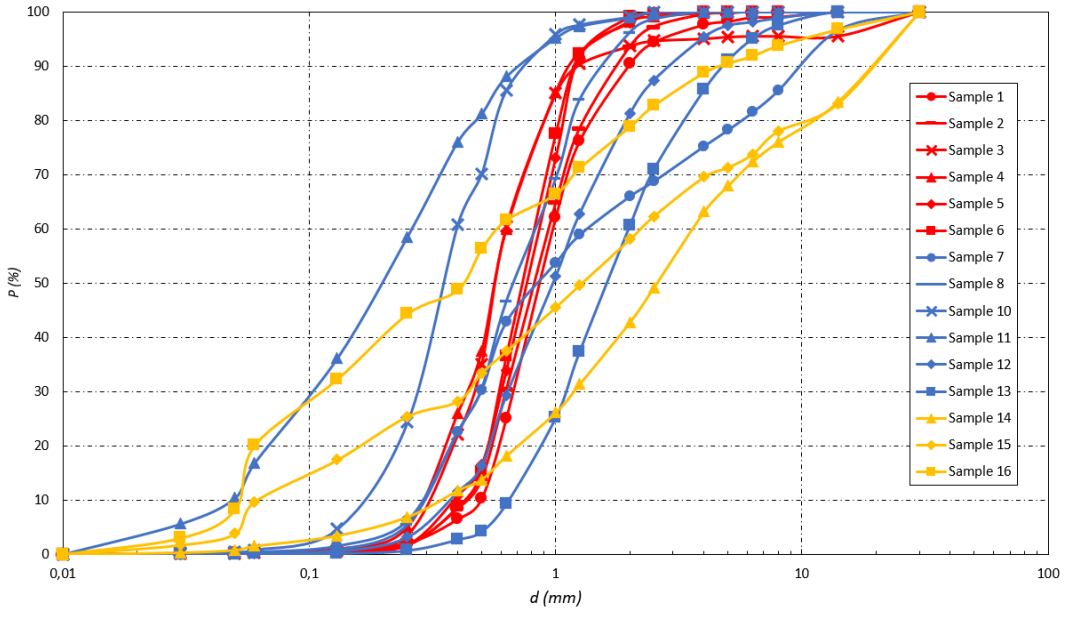

Figure 3. Measured granulometry of sediment samples (identical sample numbers between **Figures 2** and **3**).

2.2. Flow Velocity

One of the key factors in ensuring the calibration of the software HEC-RAS is measuring the flow velocity norm at various points in the water column and cross-sections of the river. This process requires the use of two measuring instruments, the current meter (see **Figure 4a**) and the ADCP (see **Figure 5a**) [57].

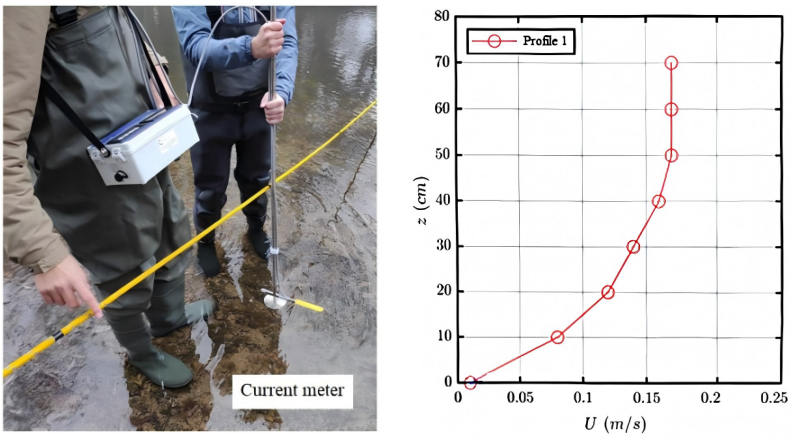

(**a**) (**b**)

Figure 4. Current meter (**a**) used to measure the norm of the flow velocity U (m/s) along a vertical profile (**b**).

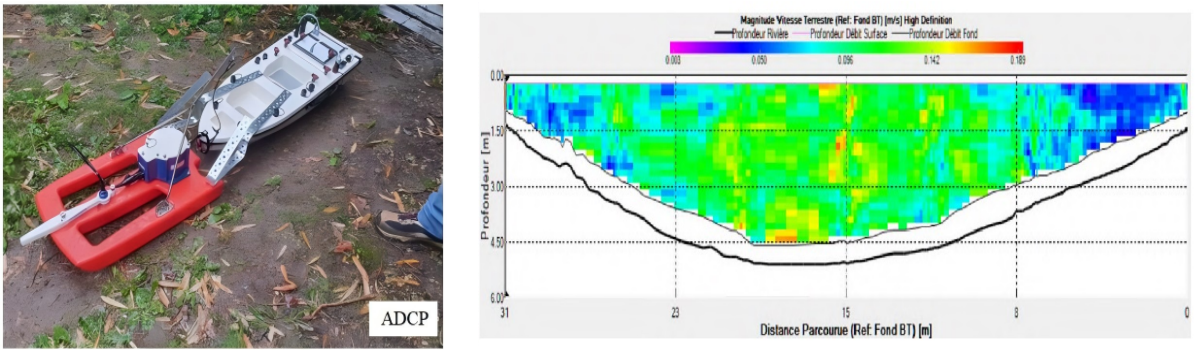

(**a**) (**b**)

Figure 5. ADCP (**a**) used to measure the norm of the flow velocity U (m/s) on a cross section (**b**).

The current meter allows manual measurement of the flow velocity norm at various points in the water column within the river (see **Figure 4a**). In this work, the current meter EMC4 from COMETEC was used, with a precision of ±0.005 m/s and a measuring range between 0 and 4 m/s. Its operation is based on the principle of electromagnetic induction, which allows it to measure the velocity norm. The current meter includes a rod with the measuring sensor attached. The operator can walk into the river, position the current meter at predetermined points, and lower the sensor vertically to measure the velocity norm at different depths at the same point. In this way, a vertical profile of the flow velocity norm can be obtained (see **Figure 4b**). The average *Um* of the flow velocity norms (m/s) is estimated using the following formula: $U_m = 0.25\ (U_{m,0.2} + U_{m,0.8} + 2\ U_{m,0.4})$. $U_{m,0.2}$, $U_{m,0.4}$, and $U_{m,0.8}$ are averages of the water velocity norm measurements at 20%, 40%, and 80% of the water depth, respectively.

The ADCP consists of a sensor attached to a drone boat, which navigates across the river while sending measurement data to a connected computer (see **Figure 5a**). The ADCP is a sophisticated tool used to measure flow velocity norms in rivers and other watercourses. It uses Doppler technology to obtain measurements of the flow velocity norm at different depths, allowing the creation of sections of flow velocity norms at various locations in the river (see **Figure 5b**). One of the main advantages of the ADCP is that it allows measuring water velocities over

a wide range of depths (up to 7 m) without deploying multiple sensors at different depths. In this work, the measurements were carried out with the TELEDYNE MARINE StreamPro ADCP, with a precision of ±1% of the water velocity. From a section of the measured flow velocity norm, information is estimated. The arithmetic mean of the flow velocity norms measured with the ADCP over a cross-section gives an overall mean flow velocity norm Umg (m/s).

2.3. DTM Maps

In this work, version 3.16 of the software QGIS was used to create the computational domain from the DTM map, which is an essential input for the software HEC-RAS. Two sources are used to obtain these DTM maps [16,58]. The first is from Grand Poitiers, and the second is from the IGN (National Institute of Geographic and Forest Information). These maps are created with a grid using a spacing of 1 m. They are produced using surveys obtained by airborne LIDAR, which has a precision of ±20–70 cm. LIDAR is a system that detects light to measure distance. The IGN DTM map has a measurement resolution ranging from 0.2 to 0.7 m in Lambert 93, which corresponds to a pixel size of 1 × 1 m [59]. The Grand Poitiers DTM map also has a resolution of 1 × 1 m in Lambert CC47.

It is important to note that the Grand Poitiers DTM maps provide accuracy concerning the riverbed, while the IGN DTM maps are distinguished by their accuracy regarding the banks [16] (see **Figure 6**). This difference is because the IGN DTM maps were created in winter, when the water level in the river is high, while the Grand Poitiers DTM maps were created when the water level is lower during low-flow conditions. Since each DTM map, Grand Poitiers and IGN, contains information that is missing from the other, merging the two DTM maps is necessary while retaining the best-represented parts of each map (see **Figure 6**). To modify the DTM map, software QGIS (Quantum Geographic Information System) is used [58]. QGIS is a user-friendly and open-source spatial software capable of processing and storing data. QGIS allows users to visualize, edit, print, and analyze geospatial data. For more complex geographic analyses, users can also utilize plugins and algorithms integrated into the software. QGIS is employed to merge the two DTM maps by leveraging its capability to combine two geospatial datasets.

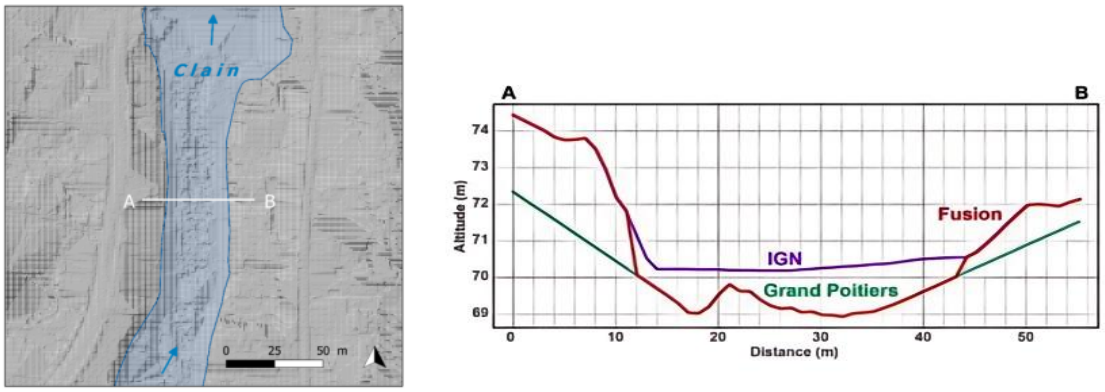

(**a**) (**b**)

Figure 6. DEM map (**a**) obtained by the fusion of DEM maps of IGN and the Grand Poitiers community, and topographic profile A-B associated (**b**).

3. Software HEC-RAS

This work uses version 6.3.1 of HEC-RAS 2D, free software not open source, developed by the U.S. Army Corps of Engineers since 2016 [48,60].

3.1. Flow Model

In HEC-RAS 2D, the river flow is governed by the averaged Shallow-Water equations with the Smagorinsky turbulence model [61,62]:

$$\frac{\partial \mathrm{h}}{\partial \mathrm{t}} + \nabla \cdot \left(h\hat{\bar{u}} \right) = 0 \quad (1)$$

$$\frac{\partial\left(h\hat{\bar{u}}\right)}{\partial \mathrm{t}} + \nabla\cdot\left(h\hat{\bar{u}}\hat{\bar{u}}\right) = -gh\frac{\partial h_O}{\partial x} - \frac{\tau_{bx}}{\rho_w} + \nabla\cdot\left(\vartheta_t\nabla\left(h\hat{\bar{u}}\right)\right) \quad (2)$$

$$\frac{\partial\left(h\hat{\bar{v}}\right)}{\partial \mathrm{t}} + \nabla\cdot\left(h\hat{\bar{v}}\hat{\bar{u}}\right) = -gh\frac{\partial h_O}{\partial y} - \frac{\tau_{by}}{\rho_w} + \nabla\cdot\left(\vartheta_t\nabla\left(h\hat{\bar{v}}\right)\right) \quad (3)$$

where h (m) is the water height, $\hat{\bar{u}}$ and $\hat{\bar{v}}$ (m/s) are the components of depth averaged velocity $\hat{\bar{u}}$, g (m/s^2) is the gravity acceleration, h_O (m) is the river bed bathymetry, τ_{bx} and τ_{by} (Pa) are the components of the shear stress τ_b, ρ_w is the water density (kg/m^3), and ν_t (m^2/s) is the turbulent viscosity. The shear stress τ_b is estimated with the Manning's formula [63]:

$$\frac{\tau_{bx}}{\rho_w} = C_D\left|\hat{\bar{u}}\right|\hat{\bar{u}}\ and\ \frac{\tau_{by}}{\rho_w} = C_D\left|\hat{\bar{u}}\right|\hat{\bar{v}}\ \text{with}\ C_D = \frac{n^2 g}{R^{\frac{1}{3}}} \quad (4)$$

where C_D is the drag coefficient, n is the Manning's roughness coefficient (s/m$^{1/3}$) and R is the hydraulic radius (m). HEC-RAS 2D uses the Smagorinsky turbulence model, a zero-equation turbulence model [42,64]. The Smagorinsky model defines turbulent viscosity as being proportional to the grid size and the velocity gradient magnitude:

$$\vartheta_t = Du_*h + (C_s\Delta)^2\left|\bar{S}\right| \text{ with } \left|\bar{S}\right| = \sqrt{2\left(\frac{\partial\bar{\tilde{u}}}{\partial x}\right)^2 + 2\left(\frac{\partial\bar{\tilde{v}}}{\partial y}\right)^2 + \left(\frac{\partial\bar{\tilde{u}}}{\partial y} + \frac{\partial\bar{\tilde{v}}}{\partial x}\right)} \quad (5)$$

where D is the dimensionless mixing coefficient tensor, u_* (m/s) is the shear velocity, Cs is the dimensionless Smagorinsky coefficient (approximately between 0.05 and 0.2), Δ (m) is the filter width equal to the local grid resolution, and $\left|\bar{S}\right|$ is the strain rate (s^{-1}). The first term Du_*h represents turbulence produced by vertical shear and the second term $(C_s\Delta)^2\left|\bar{S}\right|$ represents turbulence produced by the horizontal shear of the flow.

For the 2D flow domain to analyze unsteady flow, the software HEC-RAS utilizes two boundary conditions [65,66]. An upstream boundary condition is incorporated at the beginning of the Clain river. This upstream boundary condition is required at the upstream end of all reaches that are not connected to other reaches. It demands the flow data, provided in the form of a hydrograph, a time-series discharge file. The downstream boundary condition restricts the specific discharge at the tail end of the Clain river. It is required at the downstream end of all reaches that are not connected to other reaches. The normal depth is used to set the downstream boundary condition. It assumes that the river was flowing uniformly at the downstream boundary. The stage of each computed flow is evaluated with Manning's equation. It requires entering a friction slope. The slope of the water surface is often a good estimate of the friction slope; however, this is hard to obtain ahead of time. The average bed slope in the vicinity of the boundary condition location is often used as an estimate for the friction slope. Initial conditions were imposed at nodes located in the river by defining the starting water surface elevation.

3.2. Sediment Transport Model

HEC-RAS 2D models sediment transport using a total-load transport equation for the total concentration of sediments, where bedload and suspension are calculated within the same equation using empirical formulas [30,31]:

$$\frac{\partial}{\partial \mathrm{t}}\left(\frac{hC_{tk}}{\beta_{tk}}\right) + \nabla\cdot\left(\mathrm{h}\bar{\tilde{\boldsymbol{u}}}C_{tk}\right) = \nabla\cdot\left(\varepsilon_{tk}h\nabla C_{tk}\right) + E_{tk} - D_{tk} \quad (6)$$

where Ct_k (kg/m^3) is the total-load sediment concentration, β_{tk} is the total-load correction factor, ε_{tk} (m^2/s) is the total-load diffusion coefficient, E_{tk} (kg/m^2/s) is the total-load erosion rate in hydraulic flow, and D_{tk} (kg/m^2/s) is the total-load deposition rate in hydraulic flow for the k^{th} grain class.

The total-load horizontal diffusion coefficient ε_{tk} is determined as:

$$\varepsilon_{tk} = r_{sk}\,\varepsilon_{sk} + (1 - r_{sk})\,\varepsilon_{bk} \text{ with } \varepsilon_{sk} = \frac{C_M u_* h}{\sigma_{sk}} \text{ and } \varepsilon_{bk} = C_B u_* d_k \quad (7)$$

where r_{sk} is the fraction of suspended-load, ε_{sk} (m^2/s) is the suspended-load mixing coefficient, ε_{bk} (m^2/s) is the bed-load mixing coefficient, C_M is an empirical coefficient equal to 0.5 to 6, σ_{sk} is the Schmidt number, C_B is an empirical coefficient equal to 5, d_k (m) is the grain size diameter for the k^{th} grain class.

The total-load correction factor β_{tk} is given by:

$$\beta_{tk} = \frac{1}{r_{sk}/\beta_{sk} + (1 - r_{sk})/\beta_{bk}} \text{ with } \beta_{sk} = \frac{\int_0^h uc_k dz}{UC_k} \text{ and } \beta_{bk} = \frac{u_{bk}}{U} \quad (8)$$

where r_{sk} is the fraction of suspended sediment concentration, β_{sk} is the suspended-load correction factor, β_{bk} is the bed-load correction factor, $u_{bk}$is the bed-load velocity (m/s), U (m/s) is the depth-averaged current velocity, u (m/s) is the current velocity, C_k (kg/m^3) is the averaged sediment concentration and c_k (kg/m^3) is the current sediment concentration for the k^{th} grain class. The bed-load velocity u_{bk} is the average particle velocity during transport given by Van Rijn (1984) [67]:

$$\frac{u_{bk}}{\sqrt{R_k g d_k}} = 1.5 \max\left(\frac{\tau_b}{\tau_{crk}} - 1\right)^{0.6} \quad (9)$$

where R_k is submerged specific gravity for the k^{th} grain class, τ_b (kg/m/s^2) is grain-related bed shear stress and τcrk (kg/m/s^2) is the critical bed shear stress for the k^{th} size class.

The fraction r_{sk} of suspended sediment concentration for the k^{th} grain class is calculated using the equation of Van Rijn [67]:

$$r_{sk} = \frac{q_{sk}}{q_{tk}} = 0.25 + 0.325 \ln\left(\frac{u_*}{w_{sk}}\right) \quad (10)$$

where $q_{tk}$and $q_{sk}$are the total-load and suspended-load transport rates (kg/m/s), and w_{sk} (m/s) is the settling velocity for the k^{th} grain class.

The estimation of fractional bed changes is carried out using the Exner equation, written for each grain class:

$$\rho_{sk}(1 - \emptyset_b)\left(\frac{\partial h_0}{\partial t}\right)_k = D_{tk} - E_{tk} + \nabla\cdot(k_{bk} |q_{bk}| \nabla h_0) \text{ with } k_{bk} = 0.5\sqrt{\frac{\tau_{crk}}{max(\tau_b, \tau_{crk})}} \quad (11)$$

where ρ_{sk} (kg/m^3) is the sediment density, ϕ_b is the porosity of the eroded and deposited material, κ_{bk} is the dimensionless empirical bed slope coefficient approximately equal to 0.1 to 0.5, $|q_{bk}|$ (kg/m/s) is the mass transport rate of bedload, τ_{crk} (kg/m/s^2) is the critical shear stress for the k_{th} grain class, and τ_b (kg/m/s^2) is the bed skin shear stress. The last term on the right-hand side of the above equation accounts for bed-slope effects. The total bed change is defined as the sum of the fractional bed changes.

The total-load erosion rate E_{tk} is given by:

$$E_{tk} = f_{1k} E_{*tk} \text{ with } E_{*tk} = r_{hfa} E_{*hftk} + r_{ssa} E_{*sstk} \quad (12)$$

where f_{1k} is active grain class fractions by weight, E_{*tk} (kg/m^2/s) is potential erosion rate, r_{ssa} is the fraction of horizontal area corresponding to sheet and splash erosion, r_{hfa} is the fraction of horizontal area corresponding to hydraulic flow erosion, E_{*sstk} (kg/s/m^2) is the sheet and splash erosion potential and E_{*hftk} (kg/s/m^2) is the hydraulic flow erosion rate.

The total-load deposition rate D_{tk} in hydraulic flow is given by:

$$D_{tk} = r_{hfa} D_{tkhf} \text{ with } D_{tkhf} = \alpha_{tk} w_{sk} C_{tk} \quad (13)$$

where r_{hfa} is the fraction of horizontal area corresponding to hydraulic flow erosion, D_{tkhf} (kg/s/m^2) is the hydraulic flow deposition rate, α_{tk} is the adaptation coefficient, w_{sk}(m/s) is the sediment settling velocity and C_{tk} (kg/m^3) is the sediment concentration potential.

For the sediment transport, the equilibrium boundary condition has been used on the external boundary of the computational domain because data is not available. This boundary condition specifies the inflow sediment load as the equilibrium sediment load. The equilibrium sediment load is computed as the equilibrium sediment concentrations at the boundary cells times the face flows. This approximation essentially assumes a zero-gradient concentration normal to the boundary. Initial conditions were fixed at nodes located in the river by imposing the zero total-load sediment concentration.

4. Numerical Modeling

4.1. Flow Calibration

To calibrate the software HEC-RAS, Manning's roughness coefficient *n* (see Equation (4)) was modified several times with values ranging from 0.025 $s/m^{1/3}$ to 0.035 $s/m^{1/3}$, typical for river environments [68]. This calibration aimed to obtain flow velocities in the numerical results that closely matched field measurements across all studied cross-sections. The best-calibrated Manning's roughness coefficient *n* was 0.035 $s/m^{1/3}$. These values align with those expected for a lowland river such as the Clain [46]. A single Manning's roughness coefficient $n = 0.035\ s/m^{1/3}$ was applied uniformly across the model domain.

The first calibration was performed on the Saint-Benoît site, where a numerical simulation was conducted for a specific discharge of 4 m^3/s. The flow velocity measurements were taken at various cross-sections using the current meter (see **Figure 7c**). The second calibration took place at the Îlot Tison site, where a numerical simulation was performed for a specific discharge of 8 m^3/s. This value was measured in situ using the ADCP. The flow velocity measurements were taken at several cross-sections, both upstream and downstream of the weir (see **Figure 7b**).

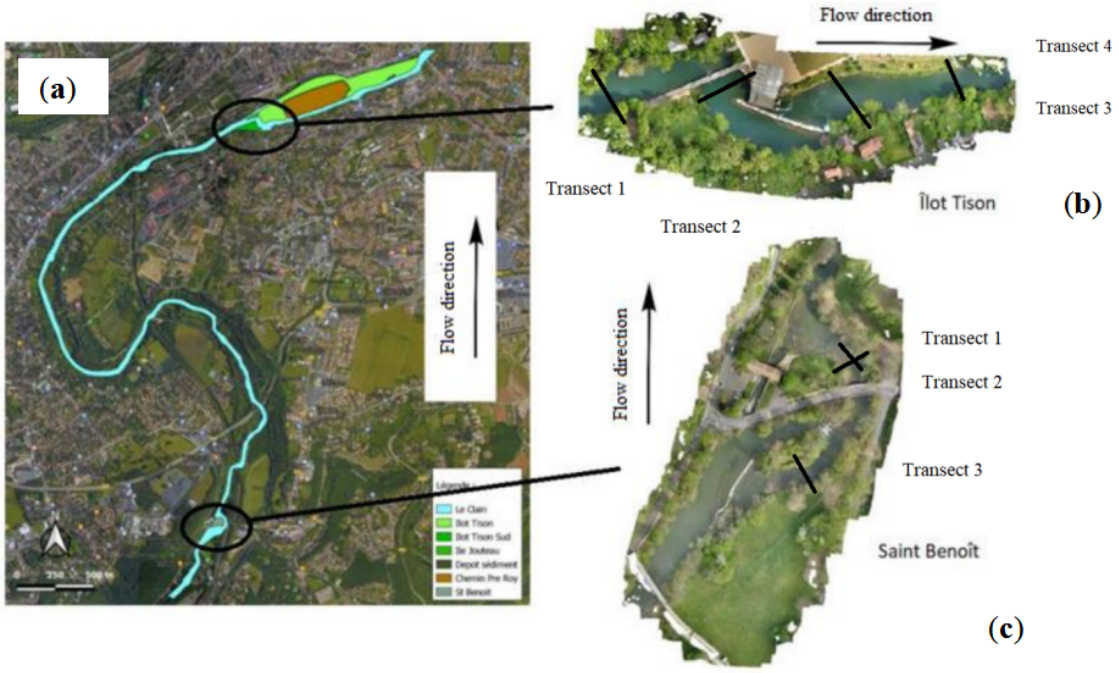

Figure 7. Global study zone (**a**), located between the two low-head dams of the Îlot Tison (**b**) and Saint-Benoît (**c**) sites, with the location of the flow velocity norm measured with the current meter on the Saint-Benoît site and the ADCP on the Îlot Tison site.

Figure 8a illustrates the average flow velocity distribution along transect 1 at the Saint-Benoît site. It demonstrates the software HEC-RAS's ability to simulate hydraulic conditions. When comparing the numerical data with actual field measurements, significant agreement was observed. The relative error, expressed as a percentage, ranged between 3% and 8%, which is considered acceptable for numerical simulations. **Figure 8b** shows the global average flow velocity *Umg* (m/s) obtained using the ADCP and HEC-RAS simulations for each cross-section at the Îlot Tison site. The remarkable consistency between the two methods confirms the validity of the numerical model and the relevance of the calibration process. The simulations successfully replicate the observed field hydraulics in a highly satisfactory manner.

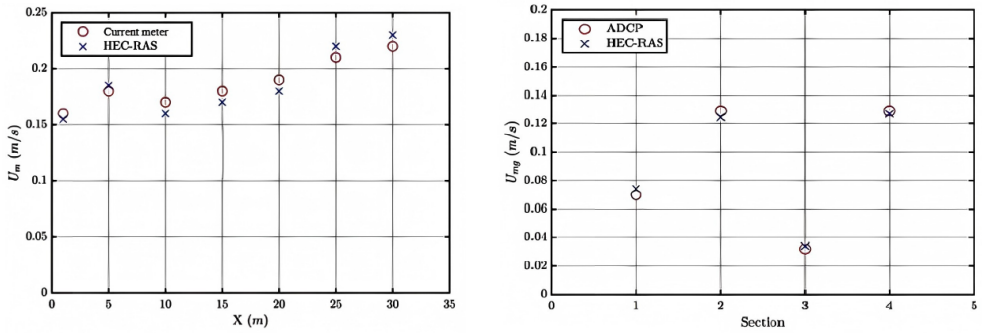

(**a**) (**b**)

Figure 8. Mean flow velocity *Um* (m/s) for the longitudinal transect 1 with a specific discharge Q = 4 m^3/s on the Saint-Benoît site (**a**) and mean global flow velocity *Umg* (m/s) for sections with a specific discharge Q = 8 m^3/s on the Îlot Tison site (**b**).
Note: red circles: field data and blue stars: HEC RAS software.

4.2. Robustness of Turbulent Models

To verify the turbulent Smagorinsky model used in the software HEC-RAS, a comparison was performed between the software HEC-RAS and the hydro-morphodynamic model HYDROSEDFOAM. HYDROSEDFOAM was developed by Zhu et al. within the OpenFOAM framework [69]. Being open-source, various turbulence models were implemented in HYDROSEDFOAM: without turbulence, the Prandtl model [38] and *k-ε* model [39]. Giving high flow velocities, the specific discharge Q = 156 m^3/s, corresponding to a ten-year flood in the Clain river, was simulated on the Îlot Tison site. **Figures 9** and **10** present the water height h and the velocity components, $\hat{\bar{u}}$ *and* $\hat{\bar{v}}$, along a transect located on the weir. The transect was chosen to cross the weir because it is at the weir that the fluctuating motions are greatest due to the presence of a waterfall (see **Figure 10**). It can be seen that the no-turbulence model and Prandtl model can lead to errors in the estimation of water height h and specific discharge Q. The two turbulence models, Smagorinsky and *k-ε*, give identical results. This numerical study complements the works of Ngatcha et al. on the consideration of turbulence in the Shallow-Water equations [34,41]. This work focuses on the Clain river, which is considered a plain river with low-head weirs. The nature of the flow is different from that studied by Ngatcha et al., hydraulic jump and dam break [34,41]. In **Figure 11**, the Froude number $Fr = U/(gh)^{1/2}$, with U (m/s) the norm of depth-averaged velocity, was estimated along the transect considered. For the specific discharge Q = 156 m^3/s, a peak in the Froude number Fr is observed at the weir due to the waterfall, without exceeding the threshold of 1.2. The turbulent water flow is supercritical only at the weir. The Clain river is in a river flow configuration rather than a torrential flow configuration. The values of Fr explain why the Smagorinsky and *k-ε* models remain robust for studying the hydro-morphodynamics of the Clain river.

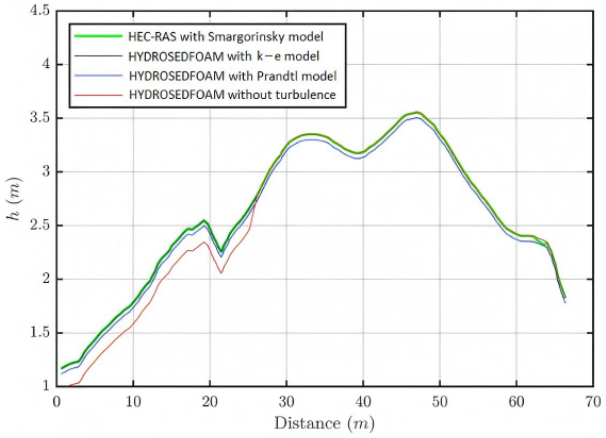

Figure 9. Water depth h along the transect obtained with different turbulent models.

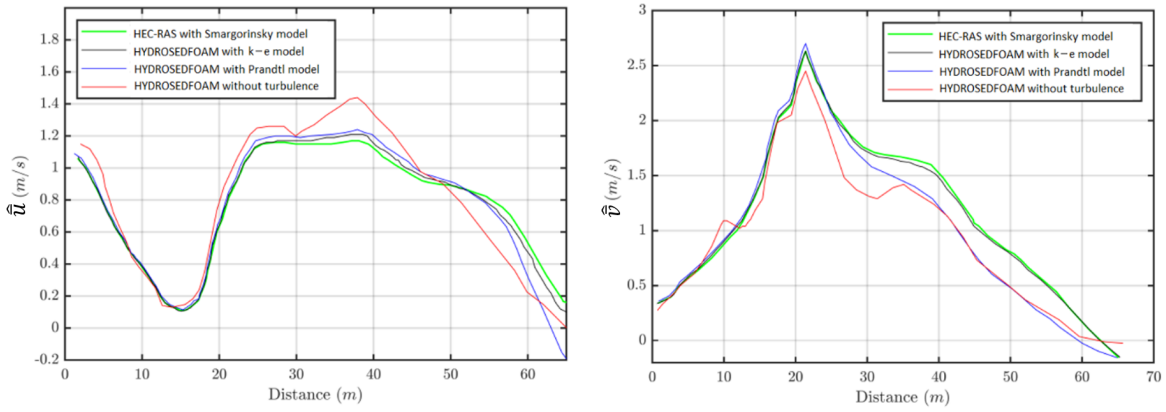

Figure 10. Components of the depth-averaged velocity, $\hat{\bar{\mathbf{u}}}$ and $\hat{\bar{\mathbf{v}}}$, along the transect obtained with different turbulent models.

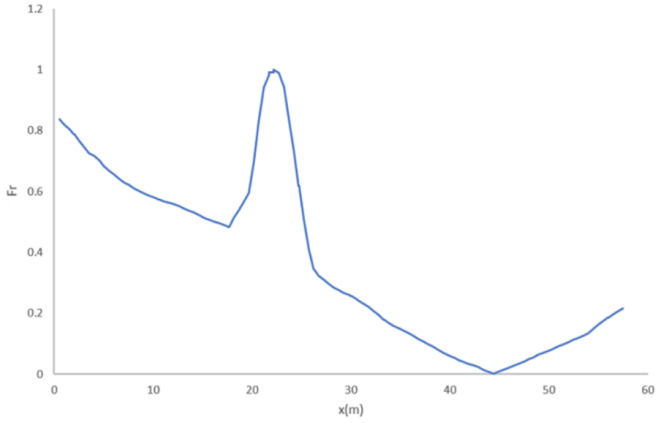

Figure 11. Froude number *Fr* along the transect.

4.3. Sediment Transport Validation

In the scientific literature, there are several empirical relations for estimating the entrainment rate *cae* of non-cohesive sediments into the river-bed for uniform material. In this work, we have compared the numerical results obtained with the software HEC-RAS to the relation developed by Van Rijn [67,70]:

$$cae = 0.015\frac{D_s}{a}\frac{S_o{}^{1.5}}{D_*{}^{0.3}} \text{ with } D_* = D_s\left(\frac{gR}{\upsilon^2}\right)^{1/3}, R = \frac{\rho_s}{\rho} - 1 \text{ and } S_o = \frac{\tau - \tau_{cr}}{\tau_{cr}} \quad (14)$$

where *Ds* (m) is the grain size, a (m) is the reference level assumed to be equal to half the bed-form height, g (9.81 m/s^2) is the gravity acceleration, $\mathcal{V}$ (10^{-6} m^2/s) is the kinematic viscosity of water, ρ_s (2650 kg/m^3) is the sediment density, ρ (1000 kg/m^3) is the water density, τ (Pa) is the bed shear stress and τ_{cr} (Pa) is the critical Shields stress. The *Ds* value is fixed to *D50* of granulometric curves of sediments samples taken between the Saint-Benoit and Îlot Tison sites, *D50* = 0.001 m (see **Figure 3**). In the numerical simulations performed with the software HEC-RAS, the thickness of the river-bed is fixed to 0.2 m, a = 0.1 m. The critical Shields stress τ_{cr} is given by the Shields diagram [71]. The bed shear stress τ is given by the numerical simulations performed with the software HEC-RAS. **Figure 12** gives the values of *cae* obtained by the Van Rijn's relation and the software HEC-RAS. To quantify the gap between the Van Rijn's relation and the software HEC-RAS, the two parameters used in the work by Garcia and Parker, mean of the discrepancy ratio *Me* and the mean absolute deviation of the discrepancy ratio *Ad*, are used here [70]:

$$Me = 10^{b1} \text{ with } b1 = \frac{1}{no}\sum_{i=1}^{no} log\left(\frac{cae\ HEC - RAS}{cae\ analytical\ solution}\right), \quad (15)$$

$$Ad=10^{b2} \text{ with } b2 = \frac{1}{no}\sum_{i=1}^{no}\left|log\left(\frac{cae\ HEC-RAS}{cae\ analytical\ solution}\right)-b1\right|. \quad (16)$$

We obtained *Me* = 1.5 and *Ad* = 2.53. It follows that perfect agreement is indicated by *Me* = 1 and *Ad* = 1. In the work by Garcia and Parker, the comparison between Van Rijn's relation and the experimental data available in the literature has given *Me* = 1.31 and *Ad* = 2.19 [70]. We can conclude that the software HEC-RAS gives a good prediction of the *cae*.

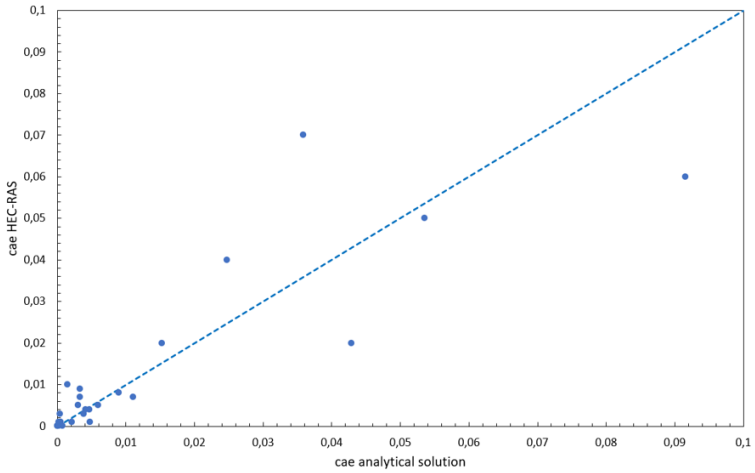

Figure 12. Comparison of numerical results obtained with the software HEC-RAS versus predictive values obtained with Van Rijn's relation.

Figure 13 presents the longitudinal profile of median grain size *D50* of river-bed material between the two low-head dams. The blue and red circles correspond to values of *D50* obtained with the granulometric curves given in **Figure 3** and the software HEC-RAS, respectively. For the measurement data, the values of *D50* are taken from samples located in the middle of the Clain river. The software HEC-RAS gives numerical results close to measurement data. We can note that the longitudinal profile is gradually changing down the river. The river-bed material is fine downstream. As sediments are carried downstream by the Clain river, sediments that characterize the river-bed material evolve, getting finer. This pattern has been well documented in natural river systems, and grain size fining is typically described as exponential [72–74]. The longitudinal profile of median grain size *D50* doesn't present discontinuities, showing thus that the sediment continuity is maintained between the two low-head dams present on the Saint-Benoit and Îlot Tison sites.

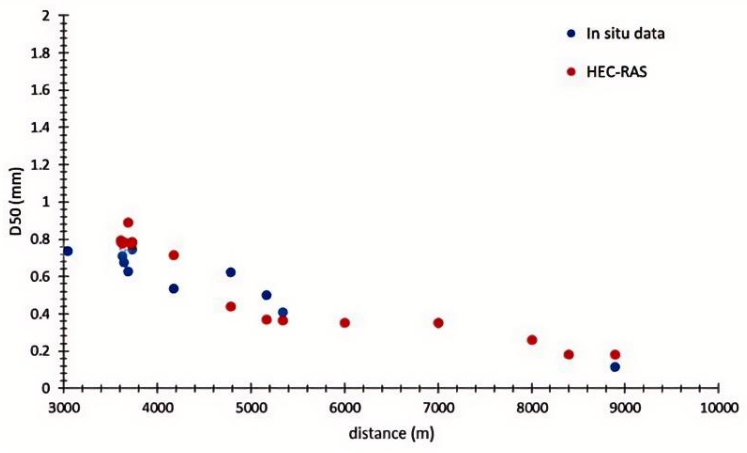

Figure 13. Longitudinal profile of the median grain size *D50*.

4.4. Scenario Development

The studied scenarios are classified into two families corresponding to two observation scales, local around low-head dams (see **Figure 7b**) and large between low-head dams (see **Figure 7a**). At the local scale, two scenarios were simulated on each site. This first scenario simulates the current conditions without modifications. This serves as a baseline for comparing the potential impacts of planned structural modifications. The second scenario simulates the situation where the low-head dam is completely removed. This hypothetical situation allows us to assess the maximum consequences of such an intervention on the hydro-morphodynamics of the Clain river. For each scenario, three specific discharges were simulated: Q = 8, 25, and 156 m^3/s. It represents a realistic range of flows encountered. The local scale allows us to understand finely how modifications to low-head dams could alter the hydro-morphodynamics of the Clain river around low-head dams, and to study the length of the Clain river 200 m on the Saint-Benoît site and 400 m on the Îlot Tison site. For the large scale, two scenarios were simulated with a specific discharge Q = 25 m^3/s. The first scenario is based on the current configuration, with the low-head dams present at the Îlot Tison and Saint-Benoît sites. This serves as the reference state. In the second scenario, the low-head dam at Îlot Tison is removed. By comparing this scenario with the current state, the impact of removing the low-head dam at Îlot Tison can be studied. The large scale allows for assessing the impact of modifications to the low-head dam at Îlot Tison on the hydro-morphodynamics of the Clain river between the two low-head dams, studied length of the Clain river 6000 m.

For all the scenarios, the river bed is assumed to be composed of sand, based on granulometry from samples taken directly at the sites, according to the existing data (see **Figure 3**). Not having information, the bed is arbitrarily fixed to 0.20 m thick with an equilibrium condition at the inlet. Regarding the hydrographs of water depth h and specific discharge Q on the Clain river available on the website of the French agency Vigicrues (https://www.vigicrues.gouv.fr), a simulated real-time of 7 days is sufficient to observe the hydro-morphodynamics of the Clain river. Performing numerical simulations is time-consuming. In order to reduce the time cost of this modeling, the software HEC-RAS allows the use of a morphological acceleration factor [48]. Assuming that morphodynamic evolution occurs at longer time scales than the hydrodynamic processes, the morphologic acceleration factor applies a scalar multiplier to the sediment transport equations [75–77]. From a sensitivity study, a morphological acceleration factor of 8 was fixed, reducing the CPU (Central Processing Unit) time while maintaining the hydro-morphodynamics of the Clain river. For the computational domain, the mesh used is composed of 47,000 cells for the Îlot Tison site, 14,000 cells for the Saint-Benoît site, and 150,000 cells for the large scale. All the numerical simulations ran on a machine equipped with two Intel(R) Xeon(R) E5-2683 v4 processors @ 2.GHz, with 25GB of RAM. Each processor has 16 cores. The total CPU time for all the numerical simulations is approximately 48 h for the Ilot Tison site, 16 h for the Saint-Benoît site, and 7 days for the large scale.

5. Numerical Results

5.1. Local Scale

5.1.1. Îlot Tison Site

Regarding the spatial distribution of the flow velocity norm Um (m/s) for the current state with the different values of the specific discharge Q considered (see **Figure 14a**), zones of acceleration and deceleration of the flow velocity are observed at the upstream of the low-head dam, caused by natural variations in the river width. An acceleration of the flow velocity is locally present at the left side of the low-head dam. The velocity norm Um is 0.7, 1.5, and 2.1 m/s for the specific discharges Q = 8 (A), 25 (B), and 156 (C) m^3/s, respectively. The low-head dam causes a reduction in the river width, leading to a local acceleration of the flow velocity upstream of the low-head dam, specific discharge being maintained. When the low-head dam is removed, the flow velocity significantly increases at the low-head dam location for specific discharges Q < 25 m^3/s (see **Figure 14b**). It is induced by the decrease in the water height h. For specific discharges Q > 25 m^3/s, the presence or absence of the low-head dam disturbs the flow velocity much less. The low-head dam is bypassed for specific discharges Q exceeding 25 m^3/s. Additionally, by removing the low-head dam, the natural flow direction of the Clain river in a meander is restored. An acceleration of the flow velocity is present in the middle of the low-head dam. On the river banks, a deceleration of the flow velocity can be observed. This phenomenon is induced by the modification of the flow section at the

location of the low-head dam when the latter is removed. This phenomenon can be observed over a hundred meters before and after the location of the low-head dam.

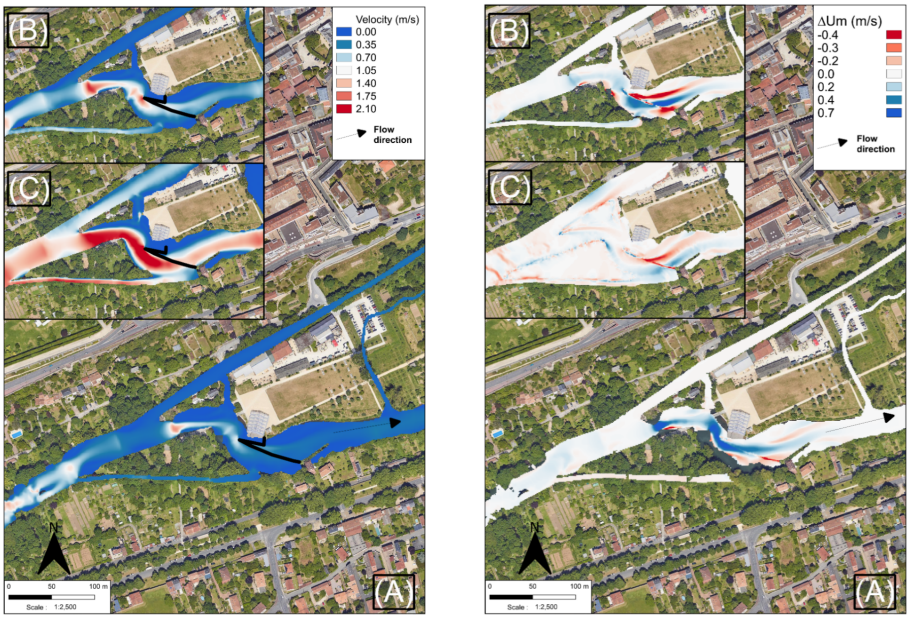

(**a**) (**b**)

Figure 14. Flow velocity norm *Um* (m/s) for the current state (**a**) and difference *ΔUm* (m/s) between the flow velocity norms with and without the low-head dam (**b**) for specific discharges Q = 8 (A), 25 (B), and 156 (C) m^3/s, on the Îlot Tison site.

In the current state, the spatial distribution of erosion ($\Delta z < 0$ m, red colors) and deposition ($\Delta z > 0$ m, blue colors) shows, upstream and downstream of the low-head dam, the natural hydro-morphodynamics of the Clain river (see **Figure 15a**). An alternation of erosion and deposition zones is observed, which is found in low-slope plains rivers whose bed consists of sands and gravels. The size of these erosion and deposition zones depends on the specific discharge Q. At the start of the low-head dam, an erosion zone is observed corresponding to the zone where there is an acceleration of the flow velocity. The eroded sediments then accumulate at the low-head dam. The intensity of this phenomenon depends on the specific discharge Q. For $Q > 25$ m^3/s, the sediment accumulation on the upstream face of the low-head dam disappears. Sediment continuity is then ensured. Without the low-head dam, the Clain river resumes its meandering river behavior (see **Figure 14b**). Erosion becomes more intense on the outer sides of bends. This erosion is more intense for specific discharges $Q < 25$ m^3/s because the presence of the low-head dam disturbs the river's hydrodynamics more for these same specific discharges. At the location of the low-head dam, an erosion zone replaces the deposition zone.

5.1.2. Saint-Benoît Site

Figure 16 presents the spatial distribution of the *Um* norm (m/s) of flow velocity in the current state (left) and the difference in the *ΔUm* norm (m/s) of flow velocity between with and without the low-head dam (right) for specific discharges Q = 8 (A), 25 (B), and 156 (C) m^3/s at the Saint-Benoît site. The spatial distribution of *Um* shows that the flow velocity is low at the upstream of the low-head dam and intensifies after the low-head dam, reaching a maximum downstream of the canoe-kayak club (see **Figure 16a**). This is explained by the river's morphology. The Clain river is wider upstream of the low-head dam, reducing its flow velocity for the same specific discharge. The spatial distribution of *ΔUm* shows that removing the low-head dam would increase the flow velocity upstream and downstream of the low-head dam (see **Figure 16b**). It is induced by the decrease in the water height h. The flow section is reduced. Unlike at the Îlot Tison site, this acceleration occurs across the entire width of the Clain river. We can also observe a deceleration of the flow velocity at the old location of the low-head dam. At the canal

passing under the canoe-kayak club, for flows exceeding 25 m^3/s, a decrease in flow velocity is observed because the river flow direction primarily shifts towards the river's main branch when the low-head dam is removed (see **Figure 16b**).

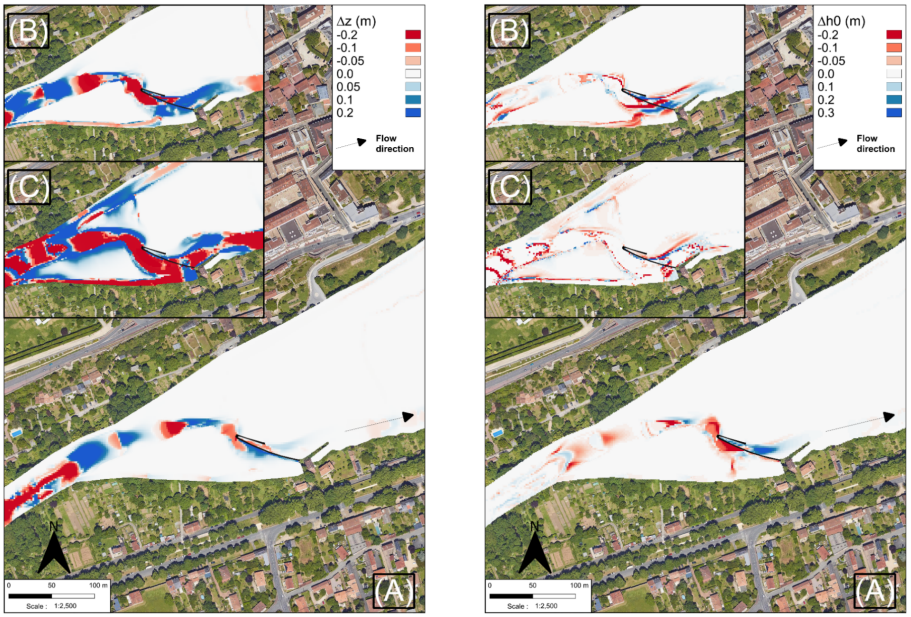

(**a**) (**b**)

Figure 15. Bathymetric variation Δz (m) with the current state (**a**) and difference $\Delta h0$ (m) between the bathymetries with and without the low-head dam (**b**) for specific discharges Q = 8 (A), 25 (B), and 156 (C) m^3/s, on the Îlot Tison site.

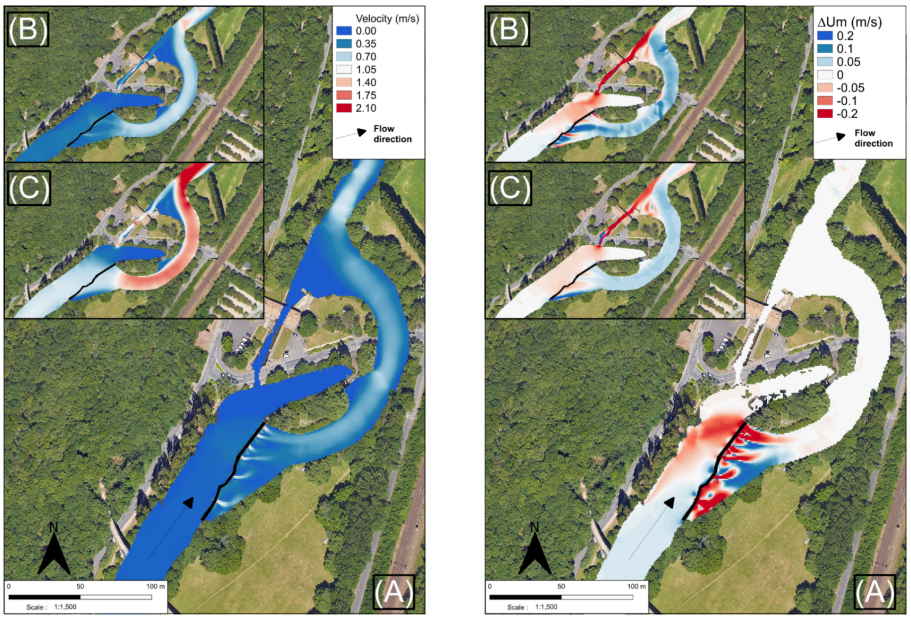

(**a**) (**b**)

Figure 16. Flow velocity norm Um (m/s) for the current state (**a**) and difference ΔUm (m/s) between the flow velocity norms with and without the low-head dam (**b**) for specific discharges Q = 8 (A), 25 (B), and 156 (C) m^3/s, on the Saint-Benoît site.

On the spatial distribution of bathymetric variation Δz (m) (see **Figure 17a**), it is observed that the zone directly upstream of the low-head dam shows a deposition zone whose intensity depends on the specific discharge. After the low-head dam, the natural hydro-morphodynamics of the Clain river resume, with an alternation of erosion and deposition zones whose size depends on the specific discharge Q. This is explained by the hydrodynamics imposed by the low-head dam. The low-head dam slows the flow upstream, creating a deposition zone upstream. Furthermore, after the low-head dam, the Clain's width narrows, causing an acceleration of the flow velocity. Regarding bathymetry differences between with and without the low-head dam (see **Figure 17b**), the spatial distribution shows a difference in the hydro-morphodynamics between discharges below and above 25 m^3/s. For specific discharges $Q < 25$ m^3/s, removing the low-head dam does not disturb the sediment transport upstream of the low-head dam location. For specific discharges $Q > 25$ m^3/s, the opposite is observed. For all the specific discharges, after the low-head dam location, a deposition zone appears.

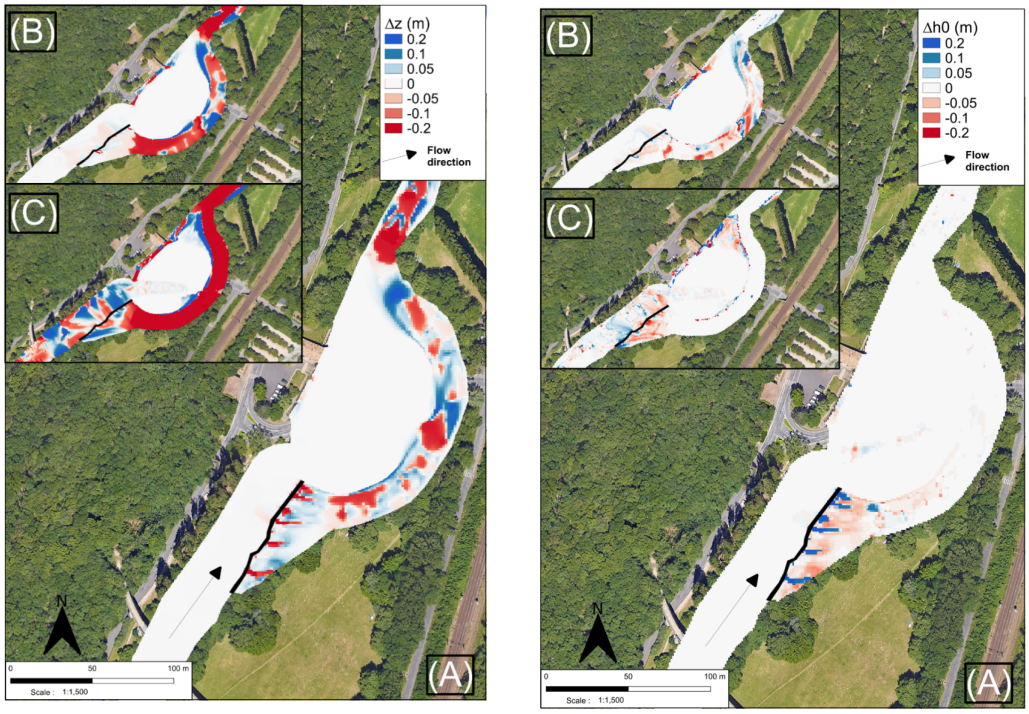

(**a**) (**b**)

Figure 17. Bathymetric variation Δz (m) with the current state (**a**) and difference $\Delta h0$ (m) between the bathymetries with and without the low-head dam (**b**) for specific discharges Q = 8 (A), 25 (B), and 156 (C) m^3/s, on the Saint-Benoît site.

5.2. Large Scale

For the current state, **Figures 18a** and **19a** present the spatial distribution of the *Um* norm (m/s) of flow velocity, and bathymetric changes Δz (m). Comparing these figures with those obtained for the same physical quantities at the local scale on the Îlot Tison and Saint-Benoît sites validates the large-scale numerical simulations. Even though the mesh between the two observation scales is not perfectly the same, it can be seen that the large-scale simulated hydrodynamics of the Clain river is the same as that simulated at the Îlot Tison and Saint-Benoît sites (see **Figure 18a** zooms on the sites). Between the two sites, the flow of a low-slope meandering plains river is observed, with zones of acceleration and deceleration of the flow velocity (see **Figure 18a**). The large-scale simulated bathymetric changes Δz at the low-head dams of the Îlot Tison and Saint-Benoît sites are identical to those simulated at the local scale for the same sites (see **Figure 19a** zooms on the sites). Between the two sites, the morphodynamics of a low-slope meandering plains river are observed. An alternation of erosion ($\Delta z < 0$ m, red colors) and deposition ($\Delta z > 0$ m, blue colors) zones is observed (see **Figure 19a**).

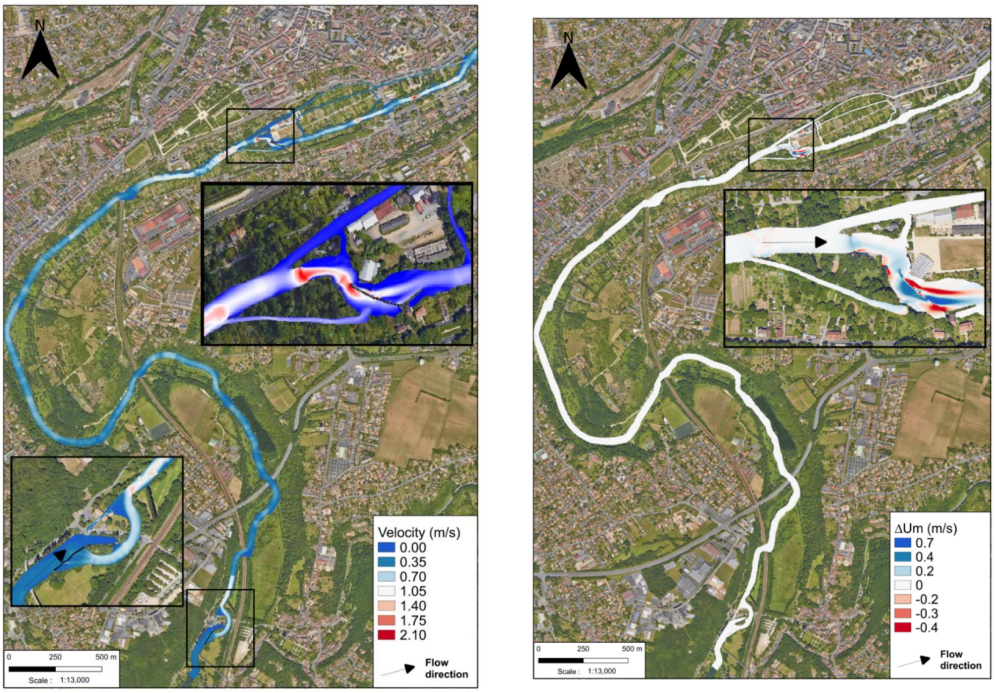

(**a**) (**b**)

Figure 18. Flow velocity norm *Um* (m/s) with the current state (a) and difference *ΔUm* (m/s) between the flow velocity norms with and without the low-head dam at the Îlot Tison site (b) for the specific discharge Q = 25 m^3/s, at the large scale.

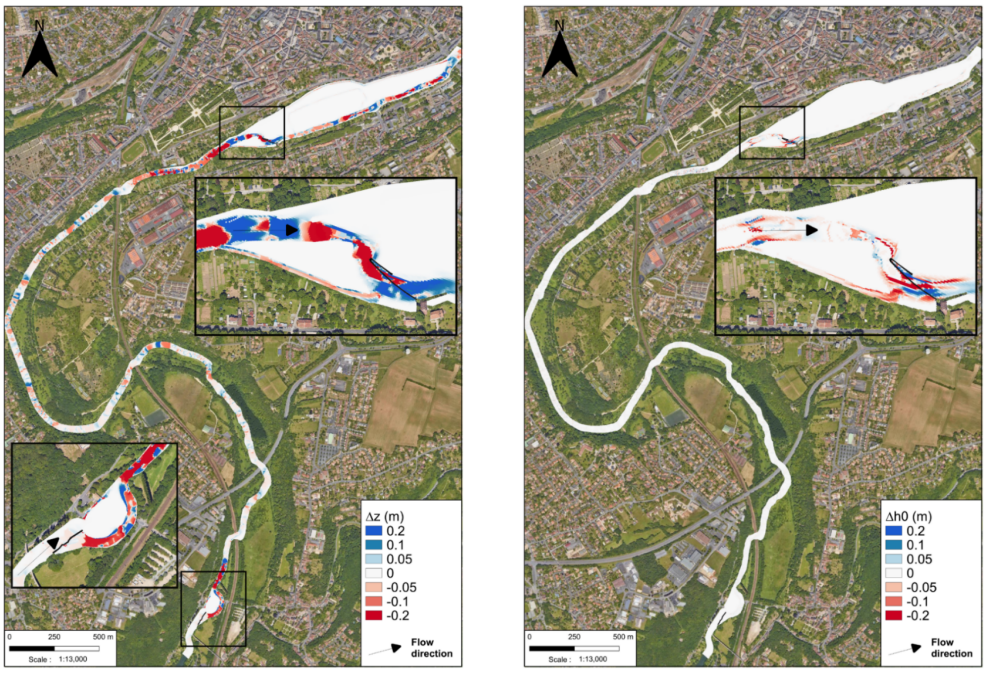

(**a**) (**b**)

Figure 19. Bathymetric variation *Δz* (m) with the current state (**a**) and difference *Δh0* (m) between the bathymetries with and without the low-head dam at the Îlot Tison site (**b**) for the specific discharge Q = 25 m^3/s, at the large scale.

In **Figures 18b** and **19b**, giving the difference maps for the flow velocity norm ΔUm (m/s), and bathymetry $\Delta h0$ (m), respectively, between with and without the low-head dam at the Îlot Tison site, it is observed that the impact of removing the low-head dam is local around the low-head dam, while there is no difference over the entire river. The Saint-Benoît site is not affected by the removal of the low-head dam at the Îlot Tison site. In **Figure 18b**, the *Um* norm of flow velocity increases in the middle of the channel at the low-head dam location after its removal, and the *Um* norm of flow velocity decreases on the sides at the same location. This observation is the same as that of the local-scale numerical simulations. By removing the low-head dam, the Clain river regains its natural flow at the meander location. In **Figure 19b**, erosion on the upstream side of the low-head dam increases, and deposition on the downstream side decreases after the low-head dam's removal. This is due to the increase in velocity at this location with the removal of the low-head dam. The impact of the low-head dam on the bathymetry $h0$ remains local around the low-head dam.

In the scientific literature, there are some works that address the problem of the low-head dam removal. In 2004, Cantelli et al. performed experiments in a canal to study the disruptions induced by a dam removal to a uniform sand bed [78,79]. An erosional narrowing (rapid reduction of channel width) was observed as soon as the dam was removed. An erosional widening (slow increase in width accompanying degradation) appeared after a second step. The erosional narrowing was interpreted as an upstream-advecting perturbation associated with a kinematic wave with finite speed along the incising channel [80]. In 2010, Ferrer-Boix et al. performed experiences similar to those of Cantelli et al. [78–80]. They studied the mechanisms observed by Cantelli et al. in a canal filled with a non-uniform sediment mixture made of sand and gravel [78,79]. The dam was composed of three slats that were sequentially removed, allowing the remaining height to control the response of the river to removal. They concluded that the upstream degradation rates can be described by a power function of a dimensionless time that accounts for water discharge and dam height. In 2003, Doyle et al. proposed a conceptual channel evolution model that summarizes the disruptions induced by a dam removal to a river bed [27]. This model was validated by following the low-head dam removal on two low gradient, fine- to coarse-grained rivers in southern Wisconsin. Doyle et al. showed that the erosional narrowing and widening are controlled by lowering of the water level and reservoir sediment characteristics. The works by Cantelli et al., Ferrer-Boix et al., and Doyle et al. are supplementary, observations based on in situ or laboratory data with different geometries of canal or river, and different characteristics of the material bed [27,78–80].

In this work, the two low-head dams studied are different. At the Saint-Benoît site, the low-head dam has a height of 1.42 m and has almost no sediments stored upstream. At the Îlot Tison site, the low-head dam has a height of 1.02 m and has a larger volume of stored sediments upstream. For the two low-head dams, a river bed composed of uniform sand was modeled with a thickness of $0.20m$ in the software HEC-RAS. Three values of the specific discharge of the Clain river were simulated, Q = 8, 25 and 156 m^3/s. For the Îlot Tison site, the erosional narrowing can be observed when the low-head dam is removed for $Q < 25$ m^3/s. If $Q > 25$ m^3/s, the low-head dam is bypassed. The presence or absence of the low-head dam disturbs the flow velocity much less. For the Saint-Benoit site, the erosional narrowing is not observed. The erosional widening appears first. In this case, there is not a volume of stored sediments upstream. The erosional widening can be observed for all specific discharges considered. This work shows that the erosional narrowing and widening are driven by the height of the removed dam, the specific discharge and the volume of stored sediments upstream.

6. Conclusions

The present work showed that the hydro-morphodynamic models, such as the software HEC-RAS, enable researchers to simulate complex sediment transport dynamics by integrating the hydrometric data such as the sediment granulometry, the flow velocity and the DMT maps. In this work, the total CPU time remained reasonable, 48 h for the Îlot Tison site, 16 hours for the Saint-Benoît site, and 7 days for the large scale, on a classic desktop workstation. The hydrometric data acquisition equipment is currently available. A Van Veen sampler, an oven and a sieve column are easy to use to obtain the sediments granulometry. Measuring flow velocity is also easily accessible from equipment such as a current meter and an ADCP. And the DTM maps data is also easily accessible in most countries. This made it possible to simulate realistic scenarios.

The numerical simulations, obtained with the software HEC-RAS, allowed us to elucidate the hydro-morphodynamic impacts of two low-head dams present at the Saint-Benoît and Îlot Tison sites, on the Grand Poitiers munici-

pality. From a hydrodynamic point of view, these low-head dams are bypassed for high specific discharges $Q > 25$ m^3/s. They only disturb the flow of the Clain river during periods of low specific discharges $Q < 25$ m^3/s, and only locally around them. Removing these low-head dams allows for the restoration of the natural flow direction of the Clain river in a meander. However, during periods of low discharges, these low-head dams help to maintain a correct water surface level in the Clain river. From a morphodynamics point of view, these low-head dams are physical barriers to the sediment transport during periods of low specific discharges $Q < 25$ m^3/s. The eroded sediments then accumulate at the low-head dams. For high specific discharges $Q > 25$ m^3/s, the flow of the Clain river is strong enough to re-establish the sediment transport above these low-head dams. Sediment continuity is then ensured. Without the low-head dams, the Clain river resumes its meandering river behavior. Removing the low-head dam at the Îlot Tison site doesn't disturb the morphodynamics of the Clain river at the Saint-Benoît site.

The numerical simulations, obtained with the software HEC-RAS, also provide practical advice in cases where a decision has to be made to remove partially or totally low-head dams. They show that the two phenomena, erosional narrowing and widening impacting the morphology of rivers around the location of dams, depend on the height of the removal dams, the specific discharge, and the volume of stored sediments upstream of the removal dams. If it is required to minimize this impact, there are alternative strategies to using explosives or heavy machinery for an immediate removal [81,82]. A partial removal allows for stabilizing upstream reservoir sediments while reducing the costs of a total removal. To prevent the dam removal, it is possible to divert the rivers around the dams if sufficient land is available. Another solution is to realize a vertical notch through the height of the dam face. All these strategies allow for the retention of some structures for historic or cultural purposes.

In the present work, the robustness of the turbulent model and sediment transport laws present in the software HEC-RAS was checked for a plain river with low-head dams, as for the Clain river. This is in accordance with the works by Ngatcha et al. [34,40,41,44,45]. The Clain river presents a Froude number $Fr < 1$, even for the ten-year flood $Q = 156$ m^3/s, and close to low-head dams. For rivers with a river (or subcritical) flow, the turbulent Smagorinsky model, introduced into the Shallow-Water equations used by the software HEC-RAS, is sufficient to simulate correctly the hydrodynamics of these rivers. For rivers with a torrential (or supercritical) flow, it will certainly be necessary to implement the second-order model developed by Ngatcha et al. in the hydro-morphodynamic models, such as the software HEC-RAS, in order to simulate correctly the hydrodynamics of these rivers [34,40,41]. In France, the major rivers, the Loire, Seine, Rhône, Garonne, and Rhin, present the two flow regimes, river and torrential. As shown by Ngatcha et al., turbulence also plays a role in sediment transport. In rivers with high fluctuating motions, the sediment transport is impacted by the distorsion and phase-lag phenomena. Ngatcha et al. have developed a new Exner equation including the phase-lag effect and arbitrary slope sediment beds [34,44,45]. This new hydro-morphodynamic model would be perfectly suited to the software BASEMENT that has recently been used to study the river morphodynamics associated with dam-breach floods. The classic coupling of Shallow-Water and Exner equations has been used to perform this study [83–85]. The recent works by Ngatcha et al. show that this coupling of Shallow-Water and Exner equations may be faulty to describe the sediment transport in flows with high fluctuating motions.

To improve the representativeness of numerical simulations performed with hydro-morphodynamic models such as the software HEC-RAS, future research should focus on the estimation of Manning's roughness n. In this work, the calibration of Manning's roughness n was performed by using hydrographs of specific discharge Q and water height h due to a lack of access to the granulometric size of the river-bed material. Since the works by Chow in 1959, the particle size-based techniques provide reasonable estimates of roughness in relatively low-gradient rivers with a gravel-sand bed because this river-bed material is the source of resistance to flow [86,87]. During low water periods, all the rivers are without water, their bed being then inaccessible. To our knowledge, there are no efficient techniques that allow access to the granulometric size of the river-bed material underwater. In a recent work, Saha et al. have used two techniques to measure the granulometric size of the river-bed material out of water [87]. They conducted the classical technique proposed by Wolman in 1954, using a zig-zag sampling approach [88]. They have taken photographs where Wolman's data were collected. Only the flawless photographs were selected for analysis with the software BASEGRAIN, allowing to perform a surface grain size study [89]. New underwater image acquisition systems and new software such as BASEGRAIN, should be developed.

Author Contributions

Conceptualization, A.G. and A.B.; methodology, A.G. and A.B.; software, A.G. and A.B.; validation, A.G. and A.B.; formal analysis, A.G. and A.B.; investigation, A.G. and A.B.; resources, A.G. and A.B.; data curation, A.G. and A.B.; writing—original draft preparation, A.G. and A.B.; writing—review and editing, A.G. and A.B. All authors have read and agreed to the published version of the manuscript.

Funding

This work received no external funding.

Institutional Review Board Statement

Not applicable.

Informed Consent Statement

Not applicable.

Data Availability Statement

Data will be made available upon request.

Conflicts of Interest

The authors declare no conflict of interest.

References

1. Fryirs, K.; Brierley, G. *Practical Applications of the River Styles Framework as a Tool for Catchment-wide River Management: A Case Study from Bega Catchment, NSW, Australia*; MacQuarie University: Auckland, New Zealand, 2005.
2. Wohl, E.; Lane, S.N.; Wilcox, A.C. The Science and Practice of River Restoration. *Water Resour. Res.* **2015**, *51*, 5974–5997. [CrossRef]
3. Reid, L.M.; Dunne, T. *Rapid Evaluation of Sediment Budgets*; *Catena*: Reiskirchen, Germany, 1996; p. 29.
4. Church, M. Geomorphic Thresholds in Riverine Landscapes. *Freshw. Biol.* **2002**, *47*, 541–557. [CrossRef]
5. Maire, A.; Laffaille, P.; Maire, J.F.; et al. Identification of Priority Areas for the Conservation of Stream Fish Assemblages: Implications for River Management in France. *River Res. Appl.* **2017**, *33*, 524–537. [CrossRef]
6. Askeyev, A.; Askeyev, O.; Askeyev, I.; et al. Predatory Fish Species as Indicators of Biodiversity: Their Distribution in Environmental Gradients in Small and Mid-Sized Rivers in Eastern Europe. *Environ. Biol. Fishes* **2021**, *104*, 767–778. [CrossRef]
7. Williams, G.P.; Wolman, M.G. *Downstream Effects of Dams on Alluvial Rivers*; US Government Printing Office: Washington, DC, USA, 1984. [CrossRef]
8. Graf, W.L. Geomorphology and American Dams: The Scientific, Social, and Economic Context. *Geomorphology* **2005**, *71*, 3–26. [CrossRef]
9. Grant, G.; Nash, C.; Selker, J.S.; et al. A Physical Framework for Evaluating Net Effects of Wet Meadow Restoration on Late Summer Streamflow. *Ecohydrology* **2018**, *11*, 1–15.
10. Schmutz, S.; Moog, O. Dams: Ecological Impacts and Management. In *Riverine Ecosystem Management: Science for Governing Towards a Sustainable Future*; *Springer*: Cham, Switzerland, 2018; pp. 111–127. [CrossRef]
11. Smith, S.G.; Muir, W.D.; Williams, J.G.; et al. Factors Associated with Travel Time and Survival of Migrant Yearling Chinook Salmon and Steelhead in the Lower Snake River. *N. Am. J. Fish. Manag.* **2002**, *22*, 385–405.
12. May, C.L.; Pryor, B.S. Initial Motion and Bedload Transport Distance Determined by Particle Tracking in a Large Regulated River. *River Res. Appl.* **2014**, *30*, 508–520. [CrossRef]
13. Dépret, T.; Piégay, H.; Dugué, V.; et al. Estimating and Restoring Bedload Transport Through a Run-of-River Reservoir. *Sci. Total Environ.* **2019**, *654*, 1146–1157. [CrossRef]
14. Csiki, S.; Rhoads, B.L. Hydraulic and Geomorphological Effects of Run-of-River Dams. *Prog. Phys. Geogr.* **2010**, *34*, 755–780. [CrossRef]
15. Kondolf, G.M.; Gao, Y.; Annandale, G.W.; et al. Sustainable Sediment Management in Reservoirs and Regulated

Rivers: Experiences from Five Continents. *Earth's Future* **2014**, *2*, 256–280. [CrossRef]
16. Beaudoin, A. Study of the Impact of the Îlot Tison Weir on Bedload Transport of the Clain River (Poitiers, France) Using BASEMENT Software. *River Res. Appl.* **2022**, *38*, 1555–1568. [CrossRef]
17. Ward, J.V.; Stanford, J.A. Ecological Connectivity in Alluvial River Ecosystems and Its Disruption by Flow Regulation. *Regul. Rivers Res. Manag.* **1995**, *11*, 105–119. [CrossRef]
18. Roni, P.; Beechie, T. *Stream and Watershed Restoration: A Guide to Restoring Riverine Processes and Habitats*; Wiley: Hoboken, NJ, USA, 2012. [CrossRef]
19. Ligon, F.K.; Dietrich, W.E.; Trush, W.J. Downstream Ecological Effects of Dams: A geomorphic perspective. *BioScience* **1995**, *45*, 183–192. [CrossRef]
20. Poff, N.L.; Allan, J.D.; Bain, M.B.; et al. The Natural Flow Regime. *BioScience* **1997**, *47*, 769–784. [CrossRef]
21. Brandt, S.A. Prediction of Downstream Geomorphological Changes After Dam Construction: A Stream Power Approach. *Int. J. Water Resour. Dev.* **2000**, *16*, 343–367. [CrossRef]
22. Rollet, A.J.; Piégay, H.; Dufour, S.; et al. Assessment of Consequences of Sediment Deficit on a Gravel River Bed Downstream of Dams in Restoration Perspectives: Application of a Multicriteria, Hierarchical and Spatially Explicit Diagnosis. *River Res. Appl.* **2014**, *30*, 939–953. [CrossRef]
23. Major, J.J.; East, A.E.; O'Connor, J.E.; et al. Geomorphic Responses to Dam Removal in the United States–A Two-Decade Perspective. In *Gravel-Bed Rivers: Processes and Disasters*; Wiley: Hoboken, NJ, USA, 2017; Volume 13, pp. 355–383.
24. Kondolf, G.M. Hungry Water: Effects of Dams and Gravel Mining on River Channels. *Environ. Manag.* **1997**, *21*, 533–551. [CrossRef]
25. Magilligan, F.J.; Roberts, M.O.; Marti, M.; et al. The Impact of Run-of-River Dams on Sediment Longitudinal Connectivity and Downstream Channel Equilibrium. *Geomorphology* **2021**, *376*, 107568. [CrossRef]
26. Pander, J.; Geist, J. Ecological Indicators for Stream Restoration Success. *Ecol. Indic.* **2013**, *30*, 106–118. [CrossRef]
27. Doyle, M.W.; Stanley, E.H.; Harbor, J.M.; et al. Dam Removal in the United States: Emerging Needs for Science and Policy. *Eos Trans. Am. Geophys. Union* **2003**, *84*, 29–33. [CrossRef]
28. Shih, W.; Diplas, P. Threshold of Motion Conditions under Stokes Flow Regime and Comparison with Turbulent Flow Data. *Water Resour. Res.* **2019**, *55*, 10872–10892.
29. Ma, H.; Nittrouer, J.A.; Wu, B.; et al. Universal Relation with Regime Transition for Sediment Transport in Fine-Grained Rivers. *Proc. Natl. Acad. Sci. USA* **2020**, *117*, 171–176. [CrossRef]
30. Shrestha, R. 2D Numerical Modelling of Sediment Diversion in a River Bend [Master's Thesis]. NTNU, Trondheim, Norway, 2022.
31. Gudgeirsdóttir, E.S. Assessment of a Sediment Management Solution in a Reservoir with a Sluicing Technique Using a HEC-RAS 2D Model: Case Study of Andakílsá River in West Iceland [Master's Thesis]. KTH Royal Institute of Technology, Stockholm, Sweden, 2023.
32. Barré de Saint Venant, A.J.C. Theory of the unsteady movement of water, with application to river floods and the introduction of tides into their beds. *Compt. Rendus Acad. Sci.* **1871**, *73*, 147–154, 237–240. (in French)
33. Gavrilyuk, S.; Ivanova, K.; Favrie, N. Multi-Dimensional Shear Shallow Water Flows: Problems and Solutions. *J. Comput. Phys.* **2018**, *366*, 252–280. [CrossRef]
34. Ngatcha, A.R.N.; Nkonga, B. A Sediment Transport Theory Based on Distortion-Free-Boundary Nonhomogeneous Fluid Flows. *Appl. Eng. Sci.* **2023**, *15*, 100148. [CrossRef]
35. Reynolds, O. IV. On the Dynamical Theory of Incompressible Viscous Fluids and the Determination of the Criterion. *Philos. Trans. R. Soc. Lond. A* **1895**, *186*, 123–164.
36. Teshukov, V.M. Gas-Dynamic Analogy for Vortex Free-Boundary Flows. *J. Appl. Mech. Tech. Phys.* **2007**, *48*, 303–309.
37. Richard, G.L.; Gavrilyuk, S.L. A New Model of Roll Waves: Comparison with Brock's Experiments. *J. Fluid Mech.* **2012**, *698*, 374–405. [CrossRef]
38. Elder, J.W. The Dispersion of Marked Fluid in Turbulent Shear Flow. *J. Fluid Mech.* **1959**, *5*, 544–560.
39. Adanta, A.; Fattah, I.M.R.; Muhammad, N.M. Comparison of Standard k-Epsilon and SST k-Omega Turbulence Model for Breastshot Waterwheel Simulation. *J. Mech. Sci. Eng.* **2020**, *7*, 39–44.
40. Duffal, V. Development of a Hybrid RANS-LES Model for the Study of Unsteady Wall Forces [Doctoral Dissertation]. Université de Pau et des Pays de l'Adour, Pau, France, 2020. Available online: https://theses.hal.science/tel-03038837v1 (in France)
41. Ngatcha, A.R.N. High Order Shallow Water Equations: Application to Dam Break Problems. *J. Mech.* **2024**, *40*, 820–842. [CrossRef]

42. Smagorinsky, J. General Circulation Experiments with the Primitive Equations: I. The Basic Experiment. *Mon. Weather Rev.* **1963**, *91*, 99–164. [CrossRef]
43. Ghzayel, A. Experimental and Numerical Studies of the Impact of Thresholds on Sedimentary Continuity [Ph.D. Thesis]. Université de Poitiers, Poitiers, France, 2023. Available online: https://theses.fr/s372096 (in French)
44. Ngatcha, A.R.N.; Bandji, D.; Njifenjou, A. Coupling of Sediment Transport Phenomena with Turbulent Surface Flows: Mathematical Modeling, Finite Volume Approximation and Test Simulations. *Eur. J. Environ. Civ. Eng.* **2024**, *28*, 3204–3237. [CrossRef]
45. Ngatcha, A.R.N. A High Order Path-Conservative Central-Upwind Arbitrary DERivative (PCCU-ADER) Method for a Generalized High Order Sediment Transport Model. *Comput. Math. Appl.* **2025**, *198*, 131–177. [CrossRef]
46. Ghani, A.A.; Zakaria, N.A.; Kiat, C.C.; et al. Revised Equations for Manning's Coefficient for Sand-Bed Rivers. *Int. J. River Basin Manag.* **2007**, *5*, 329–346.
47. Hart, D.D.; Poff, N.L. A Special Section on Dam Removal and River Restoration. *BioScience* **2002**, *52*, 653–655.
48. USACE Hydrologic Engineering Center. *HEC-RAS 2D Sediment Technical Reference Manual*; US Army Corps of Engineers: Vicksburg, MS, USA, 2023.
49. CE3E. *Étude du Devenir des Ouvrages sur le Clain de Sommières du Clain à Cenon-sur-Vienne et sur la Dive du Sud*; Clain SAGE Coordination Unit: Poitiers, France, 2016.
50. Gorin, C. Synergies of River and Land Circulation in Towns with Small Rivers: The 5 Case of Poitiers (France). *Water* **2021**, *8*, e1508. [CrossRef]
51. Brice, J.C.; Blodgett, J.C. *Countermeasures for Hydraulic Problems at Bridges. Volume II: Case Histories for Sites 1-283*; US Federal Highway Administration, Office of Research and Development: Washington, DC, USA, 1978.
52. Schumm, S.A. *The Fluvial System*; Wiley-Interscience: New York, NY, USA, 1977.
53. Syvitski, J.P. *Principles, Methods and Application of Particle Size Analysis*; Cambridge University Press: Cambridge, UK, 1991; p. 388.
54. Jodeau, C. Morphodynamique d'un Banc de Galets en Rivière Aménagée lors de Crues [Doctoral Dissertation]. Université Claude Bernard-Lyon I, Lyon, France, 2007.
55. Fournier, J.; Bonnot-Courtois, C.; Paris, R.; et al. *Analyses Granulométriques, Principes et Méthodes*; CNRS: Dinard, France, 2012.
56. Bae, J.H.; Luo, S.; Kannan, S.S.; et al. Development of an Unmanned Surface Vehicle for Remote Sediment Sampling with a Van Veen Grab Sampler. In Proceedings of OCEANS 2019 MTS/IEEE SEATTLE, Seattle, WA, USA, 27–31 October 2019; pp. 1–7. [CrossRef]
57. Hauet, A.; Morlot, T.; Daubagnan, L. Velocity profile and depth-averaged to surface velocity in natural streams: A review over alarge sample of rivers. *E3S Web Conf.* **2018**, *40*, 06015. [CrossRef]
58. Quantum Geographic Information System (QGIS). *Open Source Geospatial Foundation Project*; QGIS: Laax, Switzerland, 2022.
59. IGN. Airborne lidar: precision measurements. Available online: https://ign.fr/institut/kiosque/lidar-aeroporte-des-mesures-de-precision (accessed on 30 October 2021).
60. HEC-RAS. *River Analysis System, Hydraulic Reference Manual, Version 6.6*; US Army Corps of Engineers: Arlington, VA, USA, 2024.
61. Randall, D.A. *The Shallow Water Equations*; Department of Atmospheric Science, Colorado State University: Fort Collins, CO, USA, 2006.
62. Pilqvist, J.; Andersson, P.; Andric, J. *Tutorial–ShallowWaterFOAM*; Chalmers University of Technology: Göteborg, Sweden, 2010.
63. Esteves, M.; Faucher, X.; Galle, S.; et al. Overland Flow and Infiltration Modelling for Small Plots During Unsteady Rain: Numerical Results Versus Observed Values. *J. Hydrol.* **2000**, *228*, 265–282. [CrossRef]
64. Deardorff, J.W. A Numerical Study of Three-Dimensional Turbulent Channel Flow at Large Reynolds Numbers. *J. Fluid Mech.* **1970**, *41*, 453–480. [CrossRef]
65. Ijaz, N.; Haider, S.; Muaaz, M. Development of a Hydrodynamic Model of the Irrigation Canal Network by Using HEC-RAS: A Case Study of Layyah Canal Division, Pakistan. *Model. Earth Syst. Environ.* **2025**, *11*, 195. [CrossRef]
66. El-Haddad, B.A.; Youssef, A.M.; Karimi, Z.; Pourghasemi, H.R. Flood Inundation Mapping Using HEC-RAS 2D Modeling and Examining the Impact of Changes in the Model-Meshing Pixel Scale on the Final Output. *Water Resour. Manag.* **2025**, *39*, 5807–5826. [CrossRef]
67. Van Rijn, L.C. Sediment Transport, Part I: Bed Load Transport. *J. Hydraul. Eng.* **1984**, *110*, 1431–1456. [CrossRef]

68. Arcement, G.L.; Schneider, V.R.; et al. *Guide for Selecting Manning's Roughness Coefficients for Natural Channels and Flood Plains*; US Government Printing Office: Washington, DC, USA, 1989.
69. Zhu, Z.; LeRoy, J.Z.; Rhoads, B.L.; et al. HydroSedFoam: A New Parallelized Two-Dimensional Hydrodynamic, Sediment Transport, and Bed Morphology Model. *Comput. Geosci.* **2018**, *120*, 32–39. [CrossRef]
70. Garcia, M.; Parker, G. Entrainment of Bed Sediment into Suspension. *J. Hydraul. Eng.* **1991**, *117*, 414–435.
71. Vanoni, V.A. *Sedimentation Engineering*; ASCE Library: Reston, VA, USA, 1975.
72. Yatsu, E. On the Longitudinal Profile of the Graded River. *Trans. Am. Geophys. Union* **1955**, *36*, 655–663. [CrossRef]
73. Rice, S. The Nature and Controls on Downstream Fining Within Sedimentary Links. *J. Sediment. Res.* **1999**, *69*, 32–39. [CrossRef]
74. Dingle, E.H.; Kusack, K.M.; Venditti, J.G.; et al. The Gravel-Sand Transition and Grain Size Gap in River Bed Sediments. *Earth-Sci. Rev.* **2021**, *222*, 103838.
75. Lesser, G.R.; Roelvink, J.V.; Van Kester, J.T.M.; et al. Development and Validation of a Three-Dimensional Morphological Model. *Coast. Eng.* **2004**, *51*, 883–915. [CrossRef]
76. Morgan, J.A.; Kumar, N.; Horner-Devine, A.R.; et al. The Use of a Morphological Acceleration Factor in the Simulation of Large-Scale Fluvial Morphodynamics. *Geomorphology* **2020**, *356*, 107088. [CrossRef]
77. Balouchi, B.; Rüther, N.; Schwarzwälder, K.; et al. Temporal Variation of Braided Intensity and Morphodynamic Changes in a Regulated Braided River Using 2D Modeling and Satellite Images. *River Res. Appl.* **2024**, *40*, 708–724. [CrossRef]
78. Cantelli, A.; Paola, C.; Parker, G. Experiments on Upstream-Migrating Erosional Narrowing and Widening of an Incisional Channel Caused by Dam Removal. *Water Resour. Res.* **2004**, *40*, W03407. [CrossRef]
79. Cantelli, A.; Wong, M.; Parker, G.; et al. Numerical Model Linking Bed and Bank Evolution of Incisional Channel Created by Dam Removal. *Water Resour. Res.* **2007**, *43*, W07415. [CrossRef]
80. Ferrer-Boix, C.; Martín-Vide, J.P.; Parker, G. Channel Evolution After Dam Removal in a Poorly Sorted Sediment Mixture: Experiments and Numerical Model. *Water Resour. Res.* **2014**, *50*, 8997–9019.
81. Amos, R.A.; Annable, W.K. Upstream River Responses to Low-Head Dam Removal. In *World Environmental and Water Resources Congress 2007: Restoring Our Natural Habitat*; ASCE: Reston, VA, USA, 2007; pp. 1–8.
82. Amos, R.A. Upstream River Responses to Low-Head Dam Removal [Master's Thesis]. University of Waterloo, Waterloo, ON, Canada, 2008.
83. Chow, V.T. *Open Channel Hydraulics*; McGraw-Hill Book Co. Inc.: New York, NY, USA, 1959.
84. Graziano, A.A.; Halso, M.C.; Boes, R.M.; et al. Flood Hazard Assessment Due to Dam Breaching Considering River Morphodynamics. *Nat. Hazards* **2025**, *121*, 21633–21663.
85. Halso, M.C.; Evers, F.M.; Boes, R.M.; Vetsch, D.F. Composite Modelling of Non-Cohesive Homogeneous Spatial Dam Breaches with Varied Grain Size Distributions. *J. Hydraul. Res.* **2025**, *63*, 425–444.
86. Halso, M.C.; Evers, F.M.; Vetsch, D.F.; Boes, R.M. Effect of Grain Size Distribution in Non-Cohesive Spatial Dam Breach: Hydraulic Model Investigation and Systematic Calibration of 2D Numerical Model. *J. Hydraul. Res.* **2025**, *63*, 337–356.
87. Marcus, W.A.; Roberts, K.; Harvey, L.; et al. An Evaluation of Methods for Estimating Manning's n in Small Mountain Streams. *Mount. Res. Dev.* **1992**, *12*, 227–239. [CrossRef]
88. Wolman, M.G. A Method of Sampling Coarse River-Bed Material. *EOS Trans. Am. Geophys. Union* **1954**, *35*, 951–956.
89. Bertin, S.; Friedrich, H. Field Application of Close-Range Digital Photogrammetry (CRDP) for Grain-Scale Fluvial Morphology Studies. *Earth Surf. Process. Landf.* **2016**, *41*, 1358–1369. [CrossRef]